Research Square

Preprints are preliminary reports that have not undergone peer review.
They should not be considered conclusive, used to inform clinical practice,
or referenced by the media as validated information.

An Extended Escaping Tail of Hydrogen and Helium in a Potential Super-Earth Progenitor

Saugata Barat

saugata@mit.edu

Massachusetts Institute of Technology https://orcid.org/0009-0000-6113-0157

Shreyas Vissapragada

Carnegie Observatories

Matthew Murphy

Michigan State University

Darryl Seligman

Michigan State University

Girish Duvvuri

Vanderbilt University

Adina Feinstein

Michigan State University

Luis Welbanks

Arizona State University

William Misener

Carnegie Observatories

Sara Seager

Massachusetts Institute of Technology

Andrew Vanderburg

Harvard University

Rafael Luque

Instituto de Astrof´ısica de Andaluc´ıa

Kevin France

University of Colorado Boulder

Benjamin Rackham

Massachusetts Institute of Technology

Andrew Mann

University of North Carolina at Chapel Hill

Jean-Michel Désert

University of Potsdam

James Owen

Imperial College London
Eva-Maria Ahrer
Max Planck Insititute of Astronomy
Sagnick Mukherjee
Arizona State University
Michael Radica
University of Chicago
Matthew Nixon
Arizona State University
Keighley Rockliffe
University of Baltimore
John Livingston
Department of Astronomy, Graduate University for Advanced56 Studies (SOKENDAI)
Hinna Shivkumar
University of Amsterdam
Sydney Petz
Michigan State University

Research Article

Keywords: exoplanet atmospheres, young planets, atmospheric evolution, atmospheric escape

Posted Date: September 29th, 2026

DOI: https://doi.org/10.21203/rs.3.rs-11170492/v1

License: This work is licensed under a Creative Commons Attribution 4.0 International License.
Read Full License

Additional Declarations: The authors declare no competing interests.

An Extended Escaping Tail of Hydrogen and Helium in a Potential Super-Earth Progenitor

Saugata Barat[1,2*], Shreyas Vissapragada[3], Matthew M. Murphy[4], Darryl Z. Seligman[4], Girish M. Duvvuri[5], Adina D. Feinstein[4], Luis Welbanks[6], William Misener[7], Sara Seager[2,8,9], Andrew Vanderburg[10], Rafael Luque, Kevin France[12], Benjamin V. Rackham[8,2], Andrew W. Mann[13], Jean-Michel Désert[14,15], James E. Owen[16], Eva-Maria Ahrer[17], Sagnick Mukherjee[6,18], Michael Radica[19], Mathew C. Nixon[6,18], Keighley Rockliffe[20,21], John Livingston,23,24, Hinna Shivkumar[25] and Sydney Petz[4]

[1]Department of Astronomy, University of Texas, Austin, TX 78712, USA.

[2]Kavli Institute for Astrophysics and Space Research, Massachusetts Institute of Technology, Cambridge, MA 02139, USA.

[3]Carnegie Science Observatories, Pasadena, CA 91101, USA.

[4]Department of Physics and Astronomy, Michigan State University, East Lansing, MI 48824, USA.

[5]Department of Physics and Astronomy, Vanderbilt University, Nashville, TN 37235, USA.

[6]School of Earth and Space Exploration, Arizona State University, Tempe, AZ 85281, USA.

[7]Earth and Planets Laboratory, Carnegie Institution for Science, Washington, DC 20015, USA.

[8]Department of Earth, Atmospheric and Planetary Sciences, Massachusetts Institute of Technology, Cambridge, MA 02139, USA.

[9]Department of Aeronautics and Astronautics, Massachusetts Institute of Technology, Cambridge, MA 02139, USA.

[10]Center for Astrophysics, Harvard and Smithsonian, Cambridge, MA 02138, USA.

[11]Instituto de Astrofísica de Andalucía (IAA-CSIC), Glorieta de la Astronomía s/n, Granada, 18008, Spain.
[12]Laboratory for Atmospheric and Space Physics, University of Colorado Boulder, Boulder, CO 80309, USA.
[13]Department of Physics and Astronomy, University of North Carolina at Chapel Hill, Chapel Hill, NC, 27599, USA.
[14]Leibniz Institute for Astrophysics, AIP Potsdam, Potsdam, 14482 Potsdam, Germany.
[15]DESY, Platanenallee 6, Zeuthen, D-15738, Germany.
[16]Imperial Astrophysics, Blackett Laboratory, Imperial College London, London, SW7 2AZ, UK.
[17]Max Planck Institute for Astronomy (MPIA), Königstuhl, Heidelberg, 69117, Germany.
[18]51 Pegasi b Fellow.
[19]Department of Astronomy & Astrophysics, University of Chicago, Chicago, IL 60637, USA.
[20]Goddard Space Flight Center, NASA , Baltimore, MD 20771, USA.
[21] University of Maryland, Baltimore, MD 21201, USA.
[22]Astrobiology Center,2-21-1 Osawa, Mitaka, Tokyo 181-8588, Japan.
[23]National Astronomical Observatory of Japan,2-21-1 Osawa, Mitaka, Tokyo 181-8588, Japan.
[24]Department of Astronomy, Graduate University for Advanced Studies (SOKENDAI), Tokyo, 2-21-1 Osawa, Mitaka, Japan.
[25]Anton Pannekoek Institute for Astronomy, University of Amsterdam, Amsterdam, 1098 XH, Netherlands.

*Corresponding author(s). E-mail(s):
saugatabarat500@gmail.com;
Contributing authors: svissapragada@carnegiescience.edu;
mmmurphy@msu.edu; dzs@msu.edu; girish.duvvuri@gmail.com;
adina@msu.edu; luis.welbanks@asu.edu;
wmisener@carnegiescience.edu; seager@mit.edu;
avanderburg@cfa.harvard.edu; rluque@iaa.es;
kevin.france@colorado.edu; brackham@mit.edu;
awmann@unc.edu; jmdesert@aip.de; james.owen@imperial.ac.uk;
ahrer@mpia.de; smukhe50@asu.edu; radicamc@uchicago.edu;
matthewnixon@asu.edu; keigh.rockcliffe@gmail.com;

john.livingston@nao.ac.jp; h.shivkumar@uva.nl;
petzsydn@msu.edu;

Abstract

The loss of primordial atmospheres during the first hundred million years of planetary evolution is thought to play a fundamental role in shaping the compositional, structural and demographic properties of the most common planets in the galaxy — sub-Neptunes and super-Earths [1, 2]. Yet, empirical constraints on these early evolutionary processes remain limited. Here, we present the detection of ongoing atmospheric escape from a 23 Myr old potential super-Earth progenitor, V1298 Tau c (5.1 $R_\oplus$, 4.7 $M_\oplus$) [3], catching it in the act of shedding its primordial atmosphere. Using JWST/NIRISS SOSS observations we detect excess planetary absorption in three independent tracers of atmospheric escape simultaneously — metastable helium (1.083 μm), hydrogen Paschen-α (1.875 μm), and hydrogen Paschen-β (1.282 μm) — revealing an extended exosphere and a trailing tail of outflowing gas extending tens of planetary radii. The persistence of helium and excited hydrogen at such large distances indicates a dense hydrodynamic outflow, with a mass-loss rate exceeding $10^{\mathbf{13.5}}$ g/s and possibly a sub-solar He/H ratio ($\sim$3% solar), consistent with early evolution model predictions [4]. These data offer a powerful legacy dataset to benchmark future similar JWST observations, leveraging its unique capability of long observing baselines and simultaneous access to multiple tracers of atmospheric escape to constrain mass-loss in young transiting planets.

Keywords: exoplanet atmospheres, young planets, atmospheric evolution, atmospheric escape

One of the leading hypotheses regarding the elusive origins of the most common planets in our galaxy — super-Earths (1–1.5 $R_\oplus$) and sub-Neptunes (2–4 $R_\oplus$)[2, 5] — is the 'gas-dwarf' hypothesis [1, 6]. In this scenario, both populations of exoplanets are born with rocky cores enveloped with primordial H/He dominated atmosphere [7, 8]. These primordial atmospheres are almost completely (super-Earth) or partially (sub-Neptune) lost during the subsequent evolution ($\sim$100 Myr). There have been multiple physical processes proposed to drive this atmospheric erosion. The mass-loss could be driven by (i) deposition of energy via enhanced levels of X-ray/ultraviolet (XUV) stellar irradiation, especially during the earliest phases of the host stellar lifetime [photoevaporation; 1, 9], (ii) stellar bolometric heating, with the wind enhanced by intrinsic luminosity from the planetary interior [core-powered; 10, 11], and/or (iii) rapid expansion of the planet envelope immediately after the gas dispersal of the protoplanetary disk [boil-off; 12]. Recent studies have suggested that photoevaporation and core-powered mass loss could be working

in concert, with different mechanisms dominating at different stages of evolution [4, 13]. The relative dominance of each mechanism at different evolutionary stages has not been empirically constrained.

Transiting planets younger than 100 Myr offer an exquisite natural laboratory to measure ongoing atmospheric escape. Currently, there is a sample of ∼30 young (<100 Myr) transiting planets, and their size distribution appears consistent with gas-dwarf formation and evolution [14, 15]. Atmospheric characterization of a handful of these planets has also revealed the prevalence of low mean molecular weight atmospheres [16–19], further supporting gas-dwarf-like formation.

There exists a strong precedent of using hydrogen lines, such as Lyman-α (0.121 μm, [20–23]) and Hα (0.656 μm, [24]), as well as the metastable 1.083 μm He triplet line (1.083 μm, [25, 26]), **represented as He* throughout this manuscript,** as tracers of atmospheric escape. However, uncertainty in the physical processes that are potentially driving the atmospheric mass loss complicates how these tracers are populated, and therefore the interpretation of these observations. Specifically, constraining atmospheric mass-loss rates from observed signatures of atmospheric escape is reliant on degenerate atmospheric model parameters such as upper atmosphere temperature, mass-loss rate and H/He abundance ratio [27–29]. Observations of multiple species tracing atmospheric escape, which probe varying pressure and density regions of the outflow, could help break some of these degeneracies [30] and constrain mass-loss rates. However, such observational constraints remain elusive for young transiting planets until now.

Several studies have sought to directly detect atmospheric escape from young transiting planets (<100 Myr) using ground-based high-resolution observations, building on techniques which have been successful for mature exoplanets [31–33]. However, for young planets, these observations have yielded several non-detections [34–37] and some tentative detections [37, 38]. There is also a space-based tentative detection of escaping hydrogen reported for the 22 Myr old AU Mic b [39] using *Hubble Space Telescope* (HST) Lyman-α observations [40].

The hydrogen and helium tracers of atmospheric escape are expected to exhibit intrinsic stellar variability on hour-to-day timescales in young active stars, with amplitudes of the order of a few percent [37, 41]. Therefore, direct comparison across stellar spectra from different nights is challenging. To complicate these tantalizing but elusive mass-loss measurements even further, high mass-loss rates (which theoretically should be present on young planets) could produce extended trailing tails. These (potentially) optically-thick tails would generate transit durations for H/He lines that would be significantly longer than the broadband transit duration, as previously seen in some mature planets [42–45]. Therefore, limited temporal baselines from the ground make it challenging to completely characterize the full transit in young systems.

The challenge of limited temporal baseline can be addressed through space-based observations, as shown in the past with HST

[20, 46]. It offers a powerful alternative for detecting atmospheric escape from young planets. The James Webb Space Telescope (JWST) has successfully detected atmospheric escape in mature planets [47–49] through the He* line excess absorption using NIRISS SOSS observations. It is important to note that JWST has a significant advantage over its predecessor (HST) — due to its non-Earth centric orbit, it can observe continuously.

In this paper we report observations of a primary transit of the young potential super-Earth progenitor V1298 Tau c (23 Myr old) using JWST NIRISS/SOSS (R∼700) instrument as part of the JWST Cycle 3 large program KRONOS [PID 5959; 50]. V1298 Tau c (R=5.08±0.37 $R_\oplus$, M=4.7±0.6 $M_\oplus$) is the innermost planet in the 23 Myr old multi-planet system V1298 Tau [3, 51], with three more transiting planets beyond its orbit. It has a relatively clear, H/He dominated atmosphere [19, 52] with a low metallicity (∼15×solar) compared to mature sub-Neptunes/super-Earths [53–55]. There have been several attempts to observe the escaping atmosphere of V1298 Tau c from the ground, none of which were able to provide conclusive evidence of atmospheric escape [35, 56, 57]. Far-UV observations of V1298 Tau c with HST/COS reported significant chromospheric stellar activity but did not find any signature of escaping metals from the planetary atmosphere [58].

Our JWST observations cover both He* (1.083 μm) and multiple hydrogen Paschen (Pa) lines — **Pa-α (1.875 μm), Pa-β (1.282 μm), Pa-γ (1.094 μm) and Pa-δ (1.005 μm).** The reduction and analysis of these observations are discussed in Methods **3.1**.

1 Results

These observations have revealed the presence of a dense hydrodynamic wind (high mass-loss rate) for the young potential super-Earth progenitor V1298 Tau c. We find an extended exosphere and a trailing tail of outflowing gas, spanning ∼0.01 AU (∼2% of the planetary orbit) beyond the planet, through simultaneous detection of excess absorption in multiple tracers — He*, H Paschen α and β lines with JWST/NIRISS SOSS. We do not find evidence of excess absorption in the other Paschen lines within our bandpass.

The primary evidence for the trailing tail is apparent in the relative timing and strength of the features in our dataset. In Figure 1 we show a comparison between the timing of the broadband white light curve with the pixel-level light curves containing the He*, H Pa-α and H Pa-β lines. **We measure an excess absorption amplitude of 0.25±0.02% for He*, 0.10±0.01% for Pa-α and 0.020±0.003% for Pa-β (Methods 3.3, Extended Data Figure 2 and 3).**

The planetary ingress in the He* and H Pa-α lines occurs contemporaneously with the white light curve ingress, though the lines exhibit a significantly deeper transit, indicating an extended exosphere. The raw light curves (Figure 1) show that the dip in He* and Pa-α starts during the ingress in the white

light, continues after the fourth contact point of the white light and egress occurs ∼2 and 1.5 hours after the egress of the white light curve, respectively, providing strong evidence of the planetary origin of this absorption. **To further test this, we generate continuum subtracted light curves following the prescription outlined in [45] (Extended Data Figure 4). We find excess absorption in He* and H Pa-α during the white light curve transit, returning to pre-transit levels between 3-4 hours after the white light curve mid-transit.**

The structure of the helium and hydrogen transit — deep transit and extended absorption after the white light egress — shows that the geometry of the outflow is most similar to a trailing comet-like tail instead of being spherically symmetric. This trailing feature has been observed in a subset of mature exoplanets as well [42, 44, 45]. We fit the He*, H Pa-α**, and H Pa-**β light curves using the publicly available code `harmonica` [59] following the framework of [60] for planetary outflows. We outline the details of the light curve model and implementation in Methods Light Curve Fitting. These observations **imply** an extended tail that is **at least** 40 times longer than the broadband radius of the planet **(9.5% of the semi-major axis)** to fit the shape of the He light curve (panel C in Figure 1). Similarly, our fits **imply** that the tail in H Pa-α is ∼19 times longer than the radius of the planet **(4.7% of the semi-major axis). On the other hand, the H Pa-**β **tail is consistent with the solid body of the planet. We test the effect of potential spot crossing [61] events during our transit and the effect of smoothing (Extended Data Figure 1. We conclude that the spot crossings do not significantly affect our results. Unsmoothed `harmonica` model fits prefer an even larger outflow geometry for He*, and are consistent with the smoothed fits for Pa-α and β. Given our assumption of a simple elliptical model for a complex outflow structure, we adopt the smallest fit values (smoothed model fit, Table 1) and interpret them as lower limits.**

The trailing structure of the outflow provides evidence of a high mass-loss rate. The Paschen-α line has a short decay timescale ($\sim 10^{-8}$ s), implying that a large supply of gas sustained by high mass-loss is necessary to maintain excess absorption in these lines at such a large distance from the planet **(Methods 3.4)**. Therefore, unless the planet is vigorously losing its primordial envelope through a high density outflow, it is difficult to explain the observed excess absorptions and the long trailing tail.

Our dataset provides the unique advantage of simultaneous detection of multiple escape tracers, probing different altitudes in the outflow, which has been considered key for characterizing atmospheric escape [30, 62] — He* which has been routinely detected from ground and space [31, 44, 46]; H Pa-β, with only one confirmed detection of excess absorption in the ultra-hot Jupiter KELT-9b [63]; and H Pa-α, which has not been reported in an exoplanet atmosphere to date because it cannot be accessed from ground-based observations. We extract the transmission spectrum centered around the He*

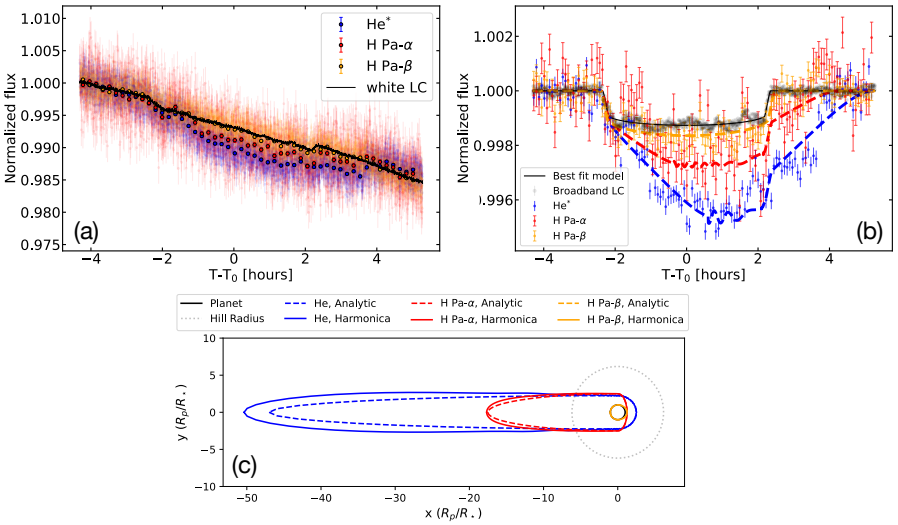


Fig. 1 Comparison between broadband white JWST NIRISS/SOSS light curve of V1298 Tau c and pixel level light curves for the **He* (blue), H Pa-α (red) and Pa-β (orange)** line demonstrating the presence of a trailing tail. (a) Raw light curves, normalized using the median of the first 100 and last 100 integrations of the visit. **The uncertainties are propagated from the stellar 1D spectra pixel level uncertainties derived from the reduction of the raw images. We bin 50 pixels for deriving the binned light curves.** (Methods 3.1). (b) Detrended light curves with best-fit models from `harmonica` (Methods 3.2) **We detrend the curvature by dividing the light curve by the best-fit baseline polynomial function and propagate the uncertainties in quadrature**. The He* and H Pa-α light curve ingress coincides with the white light curve, but the He* and H Pa-α egress occurs $\sim$2 and 1.5 hours after the end of the white light curve egress respectively. (c) **Elliptical outflow models (dashed) and the best-fit Fourier representations thereof (solid) for computing the transit light curve using `harmonica`.** The outflow extends for $\sim$40$\times$ the radius of the planet in the He* channel and for 19$\times$ the planet radius in the H Pa-α channel, indicating a dense hydrodynamic outflow. The Pa-β line, which is comparatively weaker than the Pa-α line does not show an extended tail. We show the Hill sphere for the planet in a grey dotted line. The fits shown in this figure are taken from the smoothed `harmonica` fits. We test other model assumptions in Methods 3.2 and the fit results are tabulated in Table 1.

(1.083μm), H Pa-α (1.875μm) and H Pa-β (1.282μm) from the 1D stellar spectra (Figure 2). The calculation of the transmission spectra **is** outlined in Methods 3.3. **We test the effect of 1D spectra continuum normalization width, continuum region, normalization method and temporal baseline for in-transit integrations (Extended Data Figure 2). We find that the choice of end point for the transit has the strongest effect on the measured excess absorption amplitude. We calculate the excess absorption for all three lines with different transit ends (from end of white light curve and end of He transit) and measure the average and standard deviation of the amplitude. We adopt these average values with the standard deviation as the errorbar. We further assess the impact of stellar transit light source effect (Methods 3.3) following the method outlined in [46]. We add the**

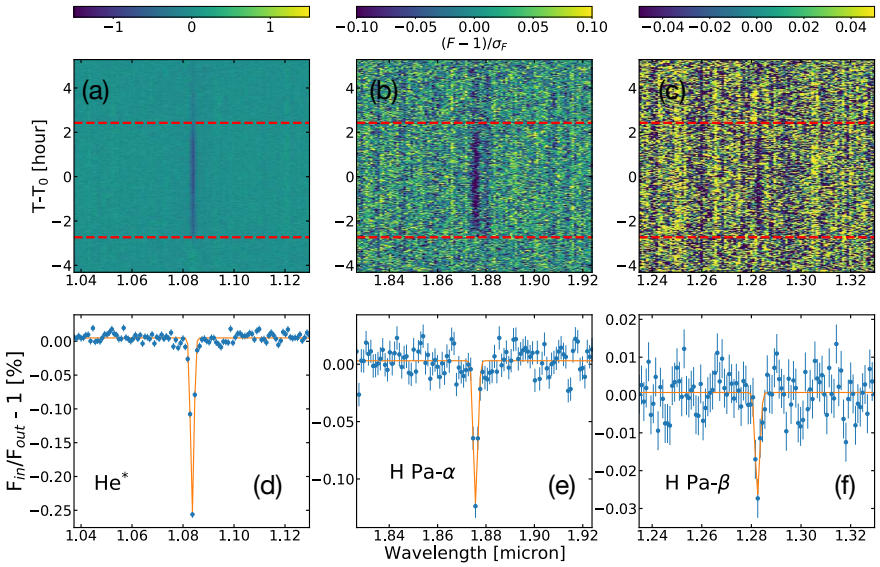


Fig. 2 Normalized stacked stellar spectra (a-c) and extracted transmission spectra (d-f) centered around the He*, H Pa-α and H Pa-β lines of V1298 Tau c respectively. The 1D spectra normalization is discussed **in** Methods 3.3. The normalized spectra have been scaled to the normalized spectra uncertainties, therefore showing SNR per integration. The red dashed lines mark the first and fourth contact points of the white light curve. Some vertical stripes are visible in the stacked spectra, which is most likely to be an outcome of residual 1/f noise correction [64]. In the lower panels the orange model shows a best-fit Gaussian profile. The blue data points have been extracted using 50 pixel half-width bins, assuming the He* light curve egress to estimate in-transit 1D spectra, normalize by fitting a straight line to the 1D spectra. All of these assumptions have been evaluated in Methods 3.3 and Extended Data Figure 2. The errorbars shown in bottom panels have been derived by measuring the RMS scatter of the residuals. The amplitude of the fitted profiles are 0.260±0.005%, 0.122±0.006% and 0.027±0.005% for the three lines respectively. The excess absorption appears at the first contact point of the transit and end ∼2.0 and 1.5 hours respectively after the fourth white light curve contact point for the He* and H Pa-α line, indicating a dense outflow. The Pa-β outflow does not extend significantly beyond the end of the white light curve egress.

uncertainty due to potential stellar unocculted spot contamination in quadrature and report an amplitude of 0.25±0.02%, 0.10±0.015% and 0.027±0.012% at the native resolution of NIRISS/SOSS for He*, H Pa-α and H Pa-β respectively.

Using a suite of numerical atmospheric outflow models we validate a high mass-loss rate implied by the observed excess absorptions and trailing tail, and constrain a conservative **lower** limit of $10^{13.5}$ g/s for V1298 Tau c. We jointly model the He*, Pa-α, and Pa-β absorption signals using `sunbather` [65]. **This software numerically solves the isothermal Parker wind model `p-winds` [67] including the 1D non-local thermodynamic equilibrium code `Cloudy` [68] to calculate the abundance of the excited states of H and He.** We generated a grid of models with mass-loss rates ranging from

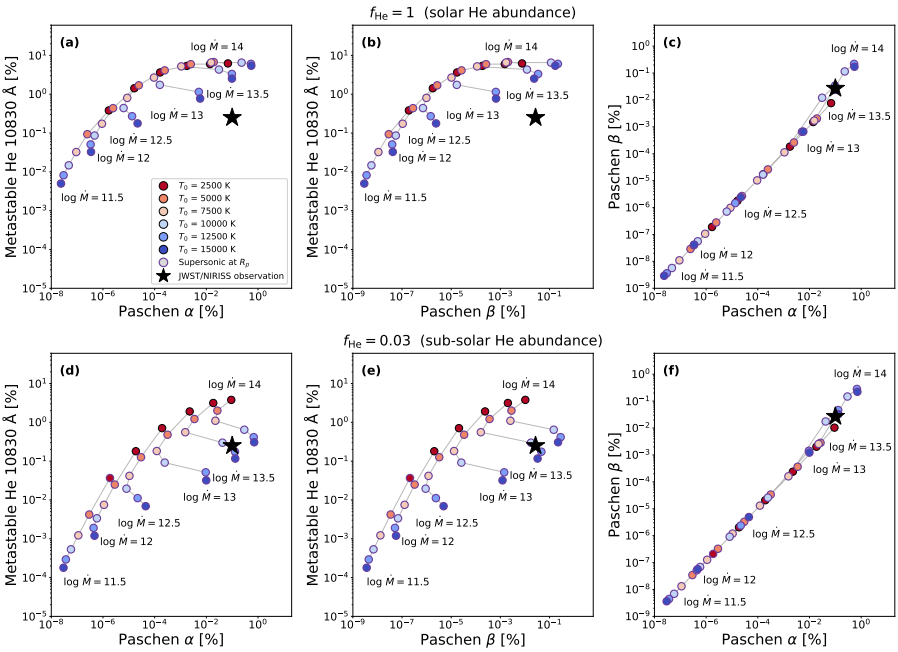


Fig. 3 Modelled excess absorption for He*, H Pa-α and H Pa-β for V1298 Tau c. We calculate a grid of models with mass-loss rates between $10^{11.5}$-10^{14} g/s and outflow initial isothermal temperature between 2500-15000 K (red to blue points) using the `sunbather` code [65], assuming a solar (a-c) and 3% solar (d-f) H/He ratio. The modelling framework is outlined in Methods 3.5. We have assumed a stellar SED from [66]. Each panel shows a correlation between two of the three tracers. The black stars show the measured excess absorption (0.25±0.02%, 0.10±0.015% and 0.027±0.012% for He*, H Pa-α and H Pa-β respectively) measured from the transmission spectra (Methods 3.3). Since the figure is shown in a log-scale, the errorbars do not appear on the figure. We find that the solar He/H ratio models do not explain both the He* and Paschen absorptions — mass-loss rates of $10^{13.5}$-10^{14} g/s explain the Paschen signal, but overpredict the He* signal. We find that a substantially lower H/He ratio (3% solar) can explain all three signals with a mass-loss rate of $10^{13.5}$ g/s with a temperature of 5000 K. Since Pa-α and β originate from the same energy level, their ratio is a constant, and it falls on a straight line (panel c and f). However, at high mass-loss rates ($10^{13.5}$-10^{14} g/s) the modeled ratios deviate due to partial saturation of the Pa-α line, which is consistent with our measured ratio. See Methods 3.5 for further details of the model.

10^{10}-10^{14} g/s, isothermal temperatures ranging from 2500–15000 K and He-to-H ratio (He/H) from 0.003-1× solar. The details of this numerical grid are outlined in Methods 3.5. In Figure 3 we show that the He* excess absorption amplitude is reasonably well-fit by both (i) moderate mass-loss rates and cool outflow temperatures ($\log \dot{M}$=12.5 and isothermal temperature of 2500 K) or (ii) high mass-loss rates and high outflow temperatures ($\log \dot{M}$=13 and isothermal temperature of 15000 K model). This is the well-known $\dot{M}$–T degeneracy [27, 28, 69], and requires independent and **complementary** information from other tracers. However, the Pa-α and β absorption signals require much higher mass-loss rates ($\log \dot{M}$=13.5-14). Furthermore, the measured ratio of Pa-α and

Pa-β absorption also supports this high mass-loss rate. The ratio of Pa-α and Pa-β absorption is expected to be constant at low gas density (Figure 3), but our measured ratio deviates from this constant exactly as expected for a dense gas with partial Pa-α saturation (Methods 3.5), supporting the high mass-loss rate interpretation in a relatively model-independent way.

However, such high mass-loss rates (10^{14} g/s) should also produce a He* absorption signal that is a factor of 10-100 larger than the observed amplitude. We explore the effect of He/H ratio in our model grid. We find that all observed amplitudes can be explained with a He/H ratio of 0.03$\times$ solar, with a mass-loss rate of $10^{13.5}$ g/s and an initial isothermal temperature of 5000 K (Figure 3). For higher He/H ratio in our grids (0.1,0.3), the He* cannot be fit, while the Pa-α and β still suggest $10^{13.5}$-10^{14} g/s. For even sub-solar He/H ratio (0.01,0.003), our grid suggests 10^{14} g/s. Therefore, we interpret these results as $10^{13.5}$ g/s as a lower limit to explain observed amplitudes of all three tracers.

It is possible that the inferred He/H ratio is lower than solar values due to a multitude of reasons such as mass fractionation [70, 71] and/or collisional de-excitation of He* by molecular hydrogen [72, 73]. These processes could reduce the expected He* absorption amplitude. For example, the mature sub-Neptune GJ436b has a strong H Ly-α detection [22], yet a non-detection in He* [31], and could be attributed to a sub-solar He/H ratio [74] or collisional de-excitation [72, 73]. **We also explored the effect of the stellar XUV radiation by scaling the spectrum from [66] by 0.1 and 10 and regenerating our models, assuming solar H/He ratio. These results are shown in Extended Data Figure 5. We find that the assumed stellar XUV flux has a moderate effect on the He* amplitude especially for low mass-loss rates. However, the Pa-α and β signals remain unaffected by the assumed stellar XUV flux. Therefore, our conclusion on the high mass-loss rate is relatively insensitive to the assumed stellar SED.**

Our conclusion of mass-loss rate greater than $10^{13.5}$ g/s is also consistent with previous tentative detections of He* and H-α excess absorption for V1298 Tau c from ground-based observations (Methods Comparison with ground-based observations and Extended Data **Figure** 7).

2 Discussion

Our results present the only simultaneous detection of multiple tracers of atmospheric escape for a young super-Earth, showing that it has an extended upper atmosphere, and a long optically thick trailing tail geometry. It provides strong empirical evidence of a hydrodynamic outflow with a high ($>10^{13.5}$ g/s) mass-loss rate, catching this planet in the act of shedding its primordial atmosphere. These results support the 'gas-dwarf' hypothesis where super-Earths and sub-Neptunes lose a significant part of their primordial envelope during the early stage of evolution, ultimately sculpting a bimodal radius distribution separated by the 'radius-valley' [2] for mature exoplanets.

Detection of multiple tracers of atmospheric escape is of utmost importance for translating these measurements into mass-loss rate constraints [62]. Stellar chromospheric lines [41] and X-ray/UV spectra [75] may vary over time for young stars, which makes the combination and comparison of multiple tracers observed at different epochs challenging. Therefore, the simultaneous detection of two tracers (He and H) of atmospheric escape using JWST demonstrates a proof-of-concept for a powerful observational strategy to study early atmospheric evolution in young planets.

As demonstrated by our observations of V1298 Tau c, the ability to observe the target for a longer duration, and simultaneous access to multiple independent tracers of escape, positions JWST ideally to characterize mass-loss from young transiting planets. These observations require no additional telescope time: broadband (0.8-2.7 μm) transmission spectra **measurements** with NIRISS/SOSS automatically provide **He*, Pa-α and Pa-β** light curves at the native resolution. While detecting extreme mass-loss and trailing tails on young exoplanets offers a tantalizing opportunity, their presence would complicate obtaining full transits from ground-based facilities. Given the variability from chromospheric lines like H-α and He* [41], using exposures from different nights to measure 'in-transit' and 'out-of-transit' stellar spectra could lead to ambiguous results, making ground-based observations challenging for such planets.

Atmospheric mass-loss rate measurements at young ages are crucial for determining the driving mechanism of atmospheric escape, since both core-powered mass-loss (CPML) and photoevaporation (PE) can explain the demographics of mature exoplanets [9, 11]. Recent theoretical calculations have demonstrated that both CPML and PE may operate in concert, but their relative dominance as a function of evolutionary stage is still an open question [13]. It has been suggested that CPML drives extreme atmospheric mass-loss at early phases when the planet is inflated while PE dominates as the planet cools and contracts [4]. We generate an evolutionary model for V1298 Tau c using the formalism outlined in [4] which includes both CPML and PE. In Figure 4 we show the mass-loss rate evolution for V1298 Tau c (4.7 $M_\oplus$, 970 K at 23 Myr). Although we cannot distinguish between CPML and PE dominated mass-loss from our mass-loss lower limit for V1298 Tau c from our observations ($10^{13.5}$ g/s), a higher mass-loss rate implied by detection of the H Pa-α and β excess absorption ($\sim 10^{14}$ g/s) could slightly prefer CPML. Although observations of a single planet are not sufficient to distinguish between these competing mechanisms empirically, similar upcoming observations of other planets in the same system (JWST GO 11831), as well as other young planets with similar age promise to provide the complementary information to test these theories.

The high mass-loss rate of V1298 Tau c would dramatically change the planetary structure in the future, if it were sustained at this vigorous level**,** and **the planet would** likely end up as a rocky super-Earth. V1298 Tau c has an envelope mass fraction of $\sim$10% [3]. Assuming a mass-loss rate of $10^{13.5}$g/s (lower limit consistent with both He* and H Paschen lines) the planet could

lose its entire envelope within the next 10 Myr and transform into a rocky super-Earth. However, we note that there are some caveats**:** the mass-loss rate may decrease as a planet contracts because XUV photons start penetrating within the sonic radius [4] and the stellar XUV irradiation decreases with time [75]. The atmospheric metallicity can change due to preferential loss of lighter elements [76, 77] and/or interior-atmosphere interactions [78–80]. There is observational evidence that the metallicity increases over time through observations of young transiting planets [17–19, 81]. Atmospheric mass-loss rate will decrease as metallicity increases due to more efficient cooling [82, 83]. Therefore, while we have observed a vigorous mass-loss rate for V1298 Tau c, further observations of other young systems spanning 10-100 Myr are needed to determine the evolution of mass-loss rate, and determine where V1298 Tau c may end up in terms of size.

The early evolution of super-Earths and sub-Neptunes is fundamental to planetary formation. However, the relevant driving mechanisms (photoevaporation and/or core-powered mass-loss) and their associated timescales [13] are still unconstrained. Furthermore, atmospheric mass-loss and compositional evolution are likely to be coupled in a non-linear way, the mechanisms of which are not yet well constrained. **Mass-loss rate constraints for V1298 Tau c from this paper will serve as a benchmark and anchor $\dot{M}$-age correlation at 23 Myr as future observations of young planets will map it out.** Measurement of atmospheric composition and mass-loss rates for planets younger than ∼100 Myr is a key step towards addressing these open questions.

3 Methods

3.1 Data reduction

The data presented in this paper consist of one primary transit of V1298 Tau c using JWST NIRISS/SOSS [85] on UT 2025 September 6 as part of the "Keys to Revealing the Origin and Nature Of sub-neptune Systems" (KRONOS) program (JWST GO 5959; PIs: Feinstein & Welbanks). We use the data reduction described and presented in [19] and summarize the key details here. Due to the brightness of V1298 Tau (J=8.687), we used SOSS with the `SUBSTRIP96` subarray which enabled time series spectroscopy from ∼0.85–2.83 μm via SOSS' first spectral order. The observation consisted of 2598 integrations over a total exposure of ∼9.6 hr, including approximately 1.92 hr of pre-transit baseline, 4.78 hr of primary transit, and 2.87 hr of post-transit baseline. These pre- and post-transit baselines were instrumental in measuring the full extent of any extended helium exosphere.

These data were reduced using the `exotedrf` reduction pipeline [86], following the standard Stages 1–3 JWST reduction routine. We performed background subtraction twice, first at the group level in Stage 1 and subsequently at the integration level in Stage 2. During the group-stage background subtraction, we did not perform differential scaling between the left and right sides of the detector. We corrected for $1/f$ noise at the group level in Stage

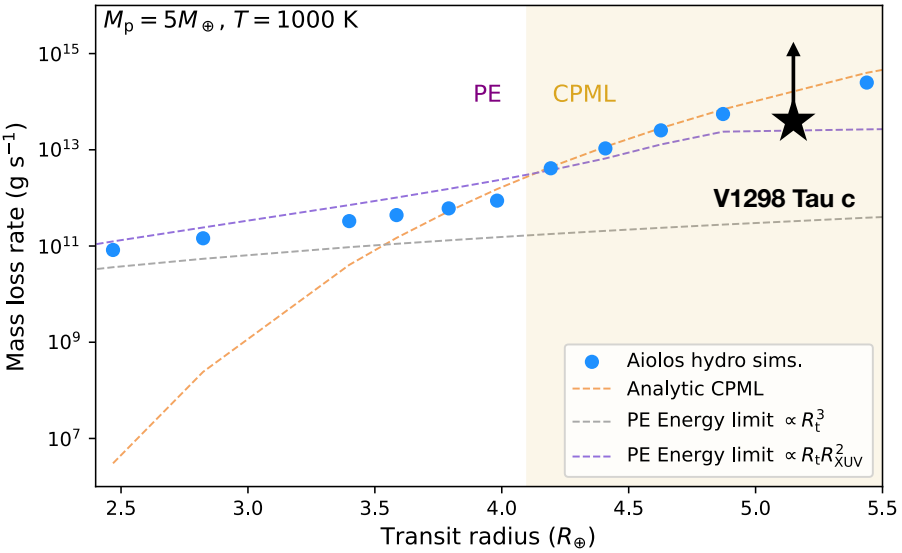


Fig. 4 The estimated mass-loss rate of V1298 Tau c ($> 10^{13.5}$g/s) is consistent with both photoevaporation and core-powered mass-loss. The mass-loss rate as a function of transit radius for a 5 $M_\oplus$ planet with an equilibrium temperature of 1000 K, assuming **an** optical-to-infrared opacity ratio of 1. The orange curve represents the analytic core-powered mass-loss model and the grey curve represents the energy limited mass-loss rate assuming the XUV radius (R_{XUV}) of the planet same as the transit radii and purple model calculates the R_{XUV} using scaling relations provided in [4]. The details of the analytical models are presented in [4]. The blue points have been calculated using the 1D hydrodynamic code `Aiolos` [84]. **We overplot the conservative mass-loss rate lower limit ($10^{13.5}$ g/s) of V1298 Tau c from our JWST observations with a black star.** Our constraints are consistent with both CPML and PE assuming $R_{XUV} > R_{transit}$.

1 using the `scale-achromatic` method, masking ±20 pixels around the spectrum during the calculation. Prior to extracting the 1D stellar spectrum, we **conducted** a Principal Component Analysis (PCA) on the time series of 2D images to identify detector and telescope artifacts using `exotedrf`'s built-in routine. We identified and removed only the beating pattern resulting from the telescope's thermal control system [e.g., 87]. We next performed a box extraction to obtain the time series of 1D stellar spectra.

3.2 Light curve fitting

We model the H and He transit light curves using `harmonica` [59], which numerically computes the transit light curve of an arbitrary shape with a spectral method. The arbitrary shape is generated via fitting coefficients for a subset of Fourier **basis** functions. We (i) model the outflow profile as an ellipse with parametric height and length, (ii) calculate the relevant Fourier coefficients with `harmonica`, and (iii) compute the corresponding light curve following the method of [60] for modeling the elliptical shape of escaping gaseous tails. `harmonica` calculates the transit light curve of custom shaped

occulting bodies by representing the projected occultor shape as a "transmission string". Ref.[60] adapted this for the specific case of escaping gas, such that the occultor takes the form of an elongated ellipse described by three parameters: l_1, the trailing tail length; l_2, the leading tail length, and h, the height of the tail. From Equation 3 of ref.[60], the total transit light curve $T_{\rm obs}$ is then computed as the sum of contributions from the gaseous tail $T_{\rm gas}$ and the planet's optical body $T_{\rm pl}$:

$$T_{\rm obs} = T_{\rm pl} + \alpha \left(T_{\rm gas} - T_{\rm pl} \right). \quad (1)$$

In Equation 1, α is a dimensionless scaling term meant to represent the opacity of the gaseous tail [60]. The planetary term $T_{\rm pl}$ is calculated in the same manner as the gaseous tail, except assuming that l_1=l_2=h=$R_p/R_\star$. For the purposes of this calculation we adopt the ratio value of $R_p/R_\star = 0.0360$ [19].

We found that our data, particularly the He light curve, required a large l_1 to l_2 ratio which results in a very elongated ellipse that requires a large number of harmonic terms (>35) in the series to adequately model. In turn, the computation of each light curve is sufficiently time-intensive and prohibitive such that standard Monte Carlo techniques would be impractical. Therefore, we use a grid-based technique to estimate the approximate shape of each gaseous outflow. We construct the parameter grid with l_1 ranging **1.0**–50.0× $R_p/R_\star$ in steps of 0.5, l_2 ranging 1.0–2.5× $R_p/R_\star$ in steps of 0.25, h ranging 1.0–2.5× $R_p/R_\star$ in steps of 0.25, and α ranging 0.02–0.07 in steps of 0.01. We calculate the light curve at each grid point using `harmonica`, assuming a transit time t_c = 60924.26916 (MJD), orbital period P = 8.2438 days, semi-major axis a = 12.21 $R_\star$, inclination i=87.8° based on ref.[19], and assuming a circular orbit with eccentricity $e = 0$ [3]. **We adopt quadratic limb-darkening with (u_1, u_2) = (0.31, 0.18) in He*, (0.11, 0.27) in H Pa-α, and (0.26, 0.22) in H Pa-β based on an ATLAS stellar model for V1298 Tau.** In this calculation we implemented 40 harmonic terms.

Another consequence of this technique in this elongated regime is that the Fourier representation can be imperfect. As a result, the tail length of a `harmonica` model for an ellipse of sufficiently large l_1 may exceed l_1 by several $R_p/R_\star$. An example of this is shown in Figure 2. The other parameters are negligibly affected by this issue as the data do not require large enough values. Therefore, the l_1 values we report from these fits should be treated as estimated lower limits.

Ref.[19] demonstrated that the out-of-transit baseline is nonlinear, and can be well fit using a cubic polynomial model. Before performing the grid fit, we first detrend the H and He light curves based on the best-fit polynomial parameters of the neighboring R=300 wavelength bins from ref.[19]. The polynomial coefficients were a_3 = 0.00117, a_2 = -0.02550, a_1 = -0.04151, and a_0 = 1.0012 for the He light curve; a_3 = 0.013130, a_2 = -0.02185, a_1 = -0.033429, and a_0 =

1.00144 for the H Pa-α light curve; **and a_3=0.031583, a_2=-0.02927, a_1=-0.03895, and a_0=1.001343 for H Pa-β,** where a_n is the coefficient for the nth order.

At higher l_2 values which are necessary to fit the observed light curve the input ellipse is sufficiently stretched that there is numerical ringing in the `harmonica` representation at localized portions of the light curve. To correct for this, we apply a Savitzky-Golay filter to the grid light curves to smooth this ringing restricted only to the affected portions of the light curve, which were typically ∼2 hr near the second-third of the gaseous transit. The transit shape in this specific region varies smoothly and is not highly sensitive to the input parameters in practice. However, for the more elongated cases, the smoothing does not always work perfectly and some ringing effect remains. The fractional difference between the smoothed and ringing-affected lightcurves is small compared to the scatter in the data. **Nevertheless, we also run a parallel case where no smoothing is done.**

Additionally, there are numerous starspot crossings during the transit that may impact our grid fits. Ref.[19] determined that these crossings affect integrations 658–850, 970–1300, 1370–1450, and 1550–1700. To understand what effect these have on our results, we run an additional case masking these integrations from the light curve, also without the Savitzky-Golay filtering. In total, we therefore run three parallel fits: (1) with the Savitzky-Golay filter, (2) without the Savitzky-Golay filter, and (3) without the Savitzky-Golay filter and with starspot crossings masked.

After computing each model light curve, we calculate the χ^2 relative to the detrended observation at each grid point. To estimate the marginalized best-fit value for each parameter, we follow the method of [88]. For each value of an individual parameter θ_i, we calculate the minimum χ^2 with all other parameters combined with that value of θ_i, then compare this to the minimum realized χ^2 value for θ_i. We estimate the uncertainty on θ_i as the range of values within $\Delta\chi^2 = 4.7$ of the minimum, based on the 68% confidence interval for a χ^2 distribution with four degrees of freedom. Extended Data Figure 1 shows the resulting marginalized $\Delta\chi^2$ profiles for **every case**.

The exact best-fit parameters for the He* light curve are case-dependent, but together suggest a significant outflow. The minimum size is for the case with light curve smoothing, with a trailing tail of $l_1 = 40.5 \pm 1.5\, R_p/R_\star$, leading tail of $l_2 = 1.5^{+0.25}_{-0.5}\, R_p/R_\star$, and height of $h = 1.5 \pm 0.25\, R_p/R_\star$. The cases without smoothing, and with spots masked, prefer either consistent or larger heights. The opacity scaler also differs, with $\alpha = 0.05 \pm 0.01$ in the smoothed case but $\alpha = 0.03 \pm 0.01$ in the unsmoothed cases.

On the other hand, the best-fit parameters for the H Pa-α and Pa-β light curves are individually highly consistent between fitting cases. For H Pa-α, the minimum best-fit l_1 is $17.5^{+4.5}_{-2.5}\, R_p/R_\star$, l_2 is not well constrained, and h is near the edge of the grid range around

2.0±0.5 $R_p/R_\star$. The opacity scaler is also near the upper edge, with α = 0.06±0.02. For H Pa-β, the outflow size is consistent with the solid body of the planet.

Given the extended tail of the escaping material, we test whether we have captured the entire egress in He* and Pa-α. Following the formalism outlined in [45], we generate continuum light curves using 25 pixel half-widths centered on these lines. We subtract it from the He* (Pa-α) light curve (Extended Data Figure 4). We see the pre-transit relative flux consistent with adjacent pixels. The He* (Pa-α) show excess absorption during the transit and go back to the pre-transit level before the visit ends. Therefore, it supports that the entire egress in He* (Pa-α) was captured during our visit.

3.3 Calculation of transmission spectrum

We normalize the stellar 1D spectrum in order to calculate the excess absorption from the planet. In this section we present the results of validation testing of two normalization techniques (referred to as **Method 1** and **Method 2**). **Method 1**: First, we select a region surrounding the He triplet (or H Pa-α and β) pixel (50 pixel half width), fit a straight line through the spectrum, and divide out with the best fit straight line. A similar method has been used for systematics detrending in ground-based high-resolution observations for He [57]. **Method 2**: We divide by the white light curve flux to remove the systematics and normalize all the spectra. We derive the transmission spectrum by taking the ratio of **the** median of the in-transit 1D spectra **to the** median **of the** out-of-transit 1D spectra**.**

The extracted transmission spectra depend on the following parameters — the normalization window (number of pixels chosen to fit straight line), assumed continuum region (whether line is masked or not for fitting straight line), temporal window for classifying in-transit integrations and the normalization method (divide by straight line or divide by white light curve). In Extended Data Figure 2 we test the dependence of the extracted transmission spectra for all three tracers on these parameters. We find that the transmission does not significantly change for different normalization windows, whether or not the line is masked, or the normalization method. It is strongly dependent on the assumed temporal window for classifying in transit integrations. We explore this further in Extended Data Figure 3, by varying the temporal window. We find that the extracted excess absorption amplitude is maximum for T_{end} (end of assumed in transit window) 3 hours after the white light mid-transit for Pa-α and Pa-β and 3.5 hours for He*. We estimate the mean and standard deviation of the excess absorption amplitude for temporal window from 2.5 hours (end of white light transit) till 4.5 hours (visual end of He transit) from the white light

mid transit. We find an excess absorption of 0.25±0.02% for He*, 0.10±0.01% for Pa-α and 0.020±0.003% for Pa-β.

We estimate the effect of stellar contamination on the measured excess absorption in He* using the formalism outlined in [46]. We assume a continuum transit depth of 1270 ppm [19]. We find the He* equivalent width of 0.45±0.05Å [41]. We find that the stellar activity contamination is 60 ppm. Our measured excess absorption is 2500±200 ppm. We add the stellar contamination uncertainty in quadrature and update the excess absorption uncertainty to 208 ppm. Performing a similar calculation for Pa-α is challenging because it is inaccessible from the ground and has no measured equivalent width. But, we can estimate the ratio of the amplitude of the He* and Paschen lines (Extended Data Figure 4), which is ∼2. As an approximation, we assume the equivalent width of the Paschen lines to be twice that of He*, i.e. 0.9Å. Using this we calculate updated errorbars for Pa-α (150 ppm) and Pa-β (123 ppm). We adopt these values as the amplitude and its uncertainty for the rest of the analysis (0.25±0.02% for He*, 0.10±0.015% for Pa-α and 0.020±0.012% for Pa-β.)

Stellar variability is not expected to cause such sharp temporal variability in the He* and Paschen line, as seen in their transit light curves, and the fact that this excess absorption is co-incident with the planetary transit is therefore strong evidence that it is not stellar. We also test the effect of the transit light source effect (TLSE) [89] on the depth of the in-transit signal in He* and Pa-α. This can affect the absolute transit depth as a function of wavelength. The detection of the trailing tail, which happens after the end of the planet transit, confirms the presence of outflowing gas, as it cannot be caused by TLSE. Therefore, to test whether any part of the signal is contaminated during the white light curve transit, we compare the ratio between He* and Paschen lines in **Extended Data** Figure 4. We find that this ratio tracks the transit, and remains the same during the white light transit and the tail-only transit, indicating **that** the TLSE does not contribute significantly to the depth of the observed transit in He* and Paschen lines.

3.4 Analytic calculation for Paschen-α

We calculate a simple analytic model for estimating the expected Pa-α signal. The Pa-α line forms from the third excited state (H=3) state, therefore the strength of the absorption depends on the population of this state. The steady state equation to determine the population of this state is given by:

$$n(H=3)A_{eff} = n(e)n(H_+)\alpha(T) + n(e)n(H=2)q_{23}(T) \quad (2)$$

where the left hand side term in Eqn 2 represents spontaneous decay, and the first term on the right hand side represents recombination and the second term represents collisional **excitation**. A_{eff} is the spontaneous decay

rate (10^8/s [90]). The relative contribution of the collisional and recombination term can be estimated using the Saha equation [91], and we find that the recombination term dominates by several orders of magnitude. We adopt the values for $\alpha(T)$ and $q_{23}(T)$ from [92] assuming a temperature of 5000 K. Therefore, Eqn 2 is reduced to,

$$n(H=3)A_{eff} = n(e)n(H_+)\alpha(T) \tag{3}$$

Assuming a fully ionized outflow, and converting number density to physical density we find that,

$$n(H=3) = \frac{\rho^2\alpha(T)}{A_{eff}} \tag{4}$$

Rewriting ρ (density) in terms of mass-loss rate and velocity of the outflow we rearrange Eqn 4,

$$n(H=3) = \frac{\dot{M}^2\alpha(T)}{16\pi^2\bar{m}^2r^4v^2A_{eff}} \tag{5}$$

We find that the Pa-α light curve tail extends till 15-20 times the planetary radii. Therefore, we assume optical depth is $\sim$1 at 15 R_p. We assume a cross section of 10^{-12}cm^2 [91]. Using this we estimate n(H=3)=43/cm^3 at 15 R_p. Putting this back in Eqn 5 we find a mass-loss rate of $\sim 10^{15}$g/s. We assume the velocity to be equal to the speed of sound, which comes to $\sim$10km/s at 5000 K. From our simple calculation we estimate a high mass-loss rate, comparable to our estimate from detailed `sunbather` models. Physically, the Pa-α state is short lived, therefore it requires a high density (mass-loss rate) to maintain such a high density of H=3 so far away from the planet.

3.5 Atmospheric escape modelling

We jointly fit the He* and Pa-α absorption signals using the sunbather code [65]. The code first models the underlying atmospheric structure using an isothermal Parker wind model from p-winds [93]. The assumption of an isothermal wind is then relaxed by solving for the heating and cooling rates with the 1D non-local thermodynamic equilibrium photoionization code Cloudy [94–96]. Once the structure converges, sunbather then calculates the planet's transmission spectrum performing radiative transfer calculations on the numerical solution. As before, we used the planetary and stellar parameters from [3] to initialize the models. We used the high-energy SED of V1298 Tau from [66], and we set the metallicity to 10×Solar, as inferred from the lower-atmospheric transmission spectrum [19].

To evaluate the agreement (or lack thereof) between model and data, we ran a grid of models spanning mass-loss rates of $\dot{M} \in (10^{10}, 10^{11}, 10^{11.5}, 10^{12}, 10^{12.5}, 10^{13}, 10^{13.5}, 10^{14})$ g s^{-1}, initial isothermal outflow temperatures of $T_0 \in (2500, 5000, 7500, 10000, 12500, 15000)$ K, and helium number density fractions (relative to solar) of $f_{\rm He} \in (1, 0.3, 0.1, 0.03, 0.01, 0.003)$. We ran sunbather for each of the grid cells and

convolved the outputted high-resolution line profile with the line-spread function of NIRISS/SOSS, which we approximated as a Gaussian at $R \sim 650$ for He*, $R \sim 700$ for Pa-β and $R \sim 850$ for Pa-α. The results from this grid are shown in Figure 3 and Extended Data Figure 6.

We were able to simultaneously match all measurements with $f_{\rm He} = 0.03$ (i.e. significant helium depletion), $\dot{M} = 10^{13.5}$ g s^{-1}, and $T_0 = 5000$ K. Figure 3 shows the model grid at $f_{\rm He} = 0.03$ compared to the observations. Our grids suggest that for even lower He/H, the required mass-loss rates appear to be $\sim 10^{14}$ g s^{-1} (Extended Data Figure 6). One salient feature is that most of the modeled outflows become supersonic at R_p. This indicates that the Parker wind model does not quite capture all of the relevant physics for this extreme planet under intense irradiation, as previously pointed out by [35]. Nevertheless, these models provide some initial context on the physical conditions of the escaping gas, which may be further developed in future work.

On its own, sunbather can fit the He* signal relatively well with a cool, weak outflow or a hot, strong outflow. This is the well-known $\dot{M}-T_0$ degeneracy [27, 28, 69]. However, the detection of the Paschen lines provides independent constraints on the structure of the planetary outflow. Only the strongest outflows are capable of populating the $n = 3$ state of hydrogen in our models: the strongest outflows have the highest densities, which results in more recombinations (and thus larger H($n = 3$) columns) in these strongly-photoionized model atmospheres. Thus, the numerical sunbather calculations match the analytic intuition developed in Section 3.4.

There is a final and model-independent constraint on the outflow density: the Pa-α/Pa-β ratio. Because both lines trace the same $n = 3$ state of neutral hydrogen, the line depth ratio is expected to be fixed (to the ratio of $f\lambda$ for each transition) in the optically-thin limit. This is why the model atmospheres in the right panel of Figure 3 fall on a single diagonal line over nearly 10 orders of magnitude. However, the observed Pa-α/Pa-β ratio deviates from this optically-thin ratio in exactly the manner expected for a dense gas, where the Paschen-α line begins to saturate. We can therefore infer that the gas through which our line-of-sight passed exhibits a high density — another indication that the mass-loss rate should be quite high. **Critically, while the He* signal depends sensitively on the high-energy SED (especially the unobservable EUV region, which plays a key role in He* radiative transfer; [26]), the Paschen ratio is fairly insensitive to the adopted SED. To test the sensitivity, we re-ran the grids with the ionizing flux ($\lambda < 912$ Å) decreased and increased by a factor of 10. Across this factor of 100 range in ionizing flux (much larger than the uncertainty on the high-energy SED), the predicted Paschen ratios change by less than 1σ at our measurement uncertainties.**

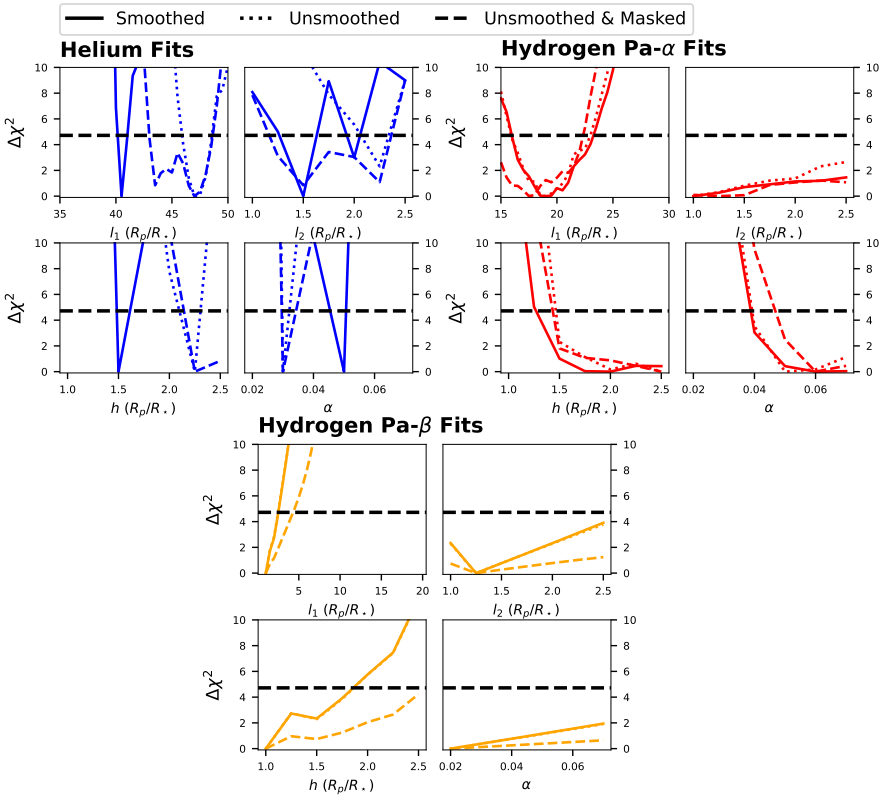
We therefore obtain a conservative mass-loss rate lower limit of $10^{13.5}$ g/s, which is required (in a relatively model-independent way)

for Paschen detectability and the observed Paschen line ratio. This is consistent with He*, albeit under the model-dependent assumption of a helium-depleted outflow $f_{\rm He} = 0.03$. While our best model is able to simultaneously fit all available data, we caution that we are essentially fitting three measurements (He*, Pa-α, Pa-β) with three free parameters ($\dot{M}$, T_0, $f_{\rm He}$). The fitting problem is underconstrained, and a good solution should be expected, but this solution is of course dependent on the physics contained within the model. A major caveat of our calculation is that we assume a spherically symmetric outflow, where in reality our observations show a long trailing tail of outflowing gas. However, previous studies have shown that modelling asymmetric outflows with 1D Parker wind models and 3D hydrodynamic outflow models produce similar order-of-magnitude constraints on mass-loss rates [28, 62, 97]. Therefore, our approach of using Parker wind models can be considered a reasonable approximation. Additionally, while the sunbather models take metal cooling into account, they do not account for the effect of molecules. Recent work has shown that significant abundance of H_2 in the outflow can suppress He* signals [30, 72]. If this were the case for V1298 Tau c, our inferred $f_{\rm He}$ would be driven higher (i.e. closer to solar). More detailed modeling efforts are needed to assess the impacts of molecules and fractionation on all three tracers simultaneously.

3.6 Comparison with ground-based observations

Ground-based He* and Hα observations for V1298 Tau c [57] are consistent with the high mass-loss rate we infer from our JWST observations. Although several ground-based observations have tried to observe the atmospheric escape of V1298 Tau c but were inconclusive [35, 56], CARMENES observations taken as part of the MOPYS survey [57] found tentative absorption signals of $\sim$4% and $\sim$2% in He* and Hα lines respectively. The detection was ambiguous as the signal was redshifted by -28km/s. A similar tentative excess H-α absorption was also reported for V1298 Tau c in [98, 99]. In Figure 7 we compare the predicted absorption strength for He* line and Hα at the resolution of CARMENES from our 1D atmospheric escape models (Methods 3.5). A mass-loss rate of 10^{13}g/s is consistent with the observed He* and Hα absorption amplitude in V1298 Tau c (for both solar and sub-solar He/H ratio), and is therefore consistent with our JWST observations. Although the pixel-to-pixel velocity resolution is much lower ($\sim$170km/s) for JWST, the longer temporal baseline and simultaneous broadband light curve allow us to distinguish between stellar variability and planetary absorption and derive an out-of-transit stellar spectrum. The ground-based observations discussed here [35, 56, 57] had either no or limited pre-transit exposures and no post He* egress observations due to limited temporal coverage. This makes deriving a reliable out-of-transit spectrum challenging for ground-based observations of

such young planets which could have long trailing tails like V1298 Tau c due to high expected mass-loss rates.



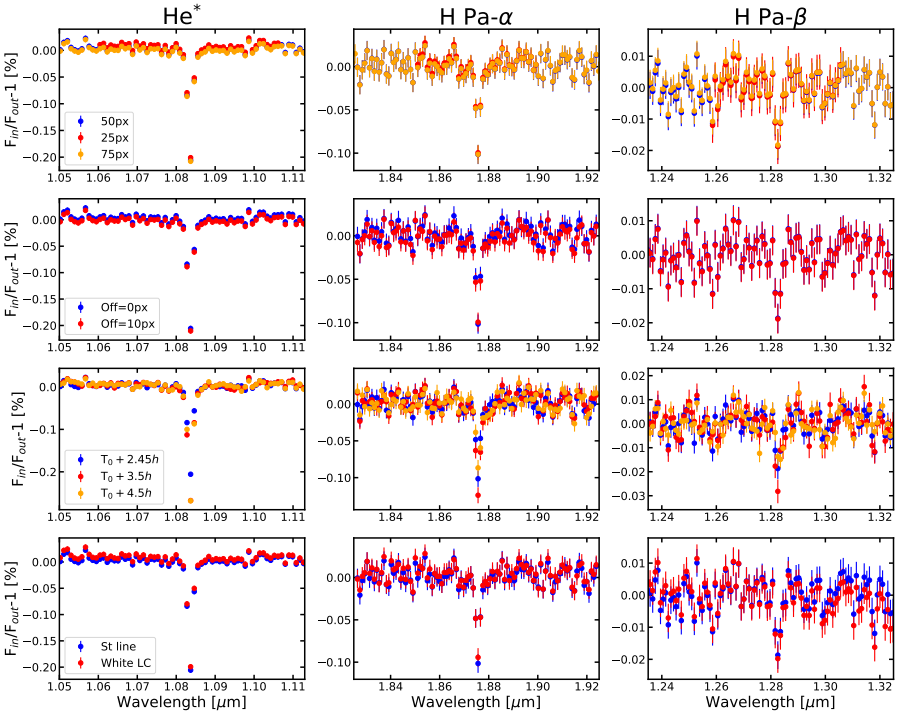
Extended Data Figure 1 Relative χ^2 profiles for each of our light curve parameters when fitting the He* (upper left, blue) and Pa-α (upper right, red) and Pa-β light curves. Solid lines represent model fits using a Savitzky-Golay filter, dotted lines represent unsmoothed model fits and dashed lines represent unsmoothed model fits where spot crossing events have been masked. The horizontal dashed line in each panel marks $\Delta\chi^2 = 4.7$, which defines the $\sim 1\sigma$ confidence interval [88]. The best fit parameters with uncertainties are shown in Extended Data Table 1. Further details are discussed in Methods 3.2.

Extended Data Figures

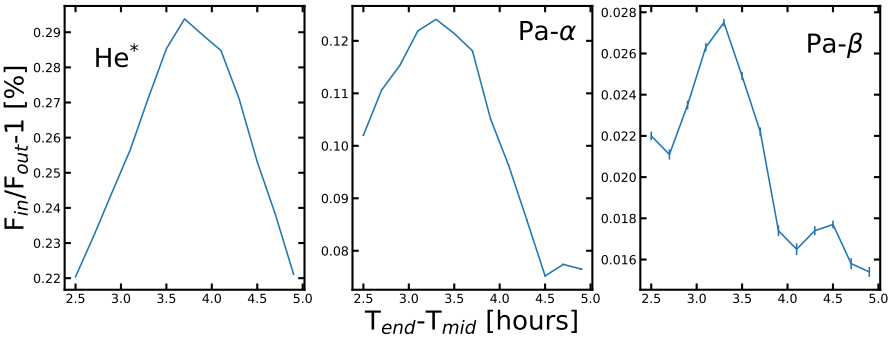
Extended Data Table

Data availability

The data used in this study may be obtained from the Mikulski Archive for Space Telescopes (MAST, https://mast.stsci.edu/) and are associated with JWST GO 5959.



Extended Data Figure 2 Comparing the effect of different spectral extraction parameters on the extracted transmission spectra for He*, Pa-α and Pa-β respectively (left to right column). The top row tests the effect of normalization window width, the second row tests the effect of masking the line while calculating the normalization model, the third row tests the effect of the temporal region selected for estimating in-transit and out-of-transit spectra and the bottom row tests different normalization **procedures** (normalization by fitting a straight line and normalization by the white light curve). The blue data points represent the reference choice for the parameters (50 pixels normalization width, no masking, T_{end}=T_0+2.45 hours and normalization by fitting a straight line). In each panel we vary one of the parameters from the reference parameter choice to test its effect. We note that for the in-transit duration, we assume that the transit starts at 2.45 hours before the mid-transit time (T_0=60924.268889 MJD), assuming a transit duration of 4.9 hours [3]. We find that varying the normalization region from 25-75 pixels (half-width) does not affect the extracted transmission spectra significantly. Similarly, whether the spectral lines are masked or not while fitting the straight line through the normalization window, or whether we normalize the stellar spectra using the white light curve flux does not seem to have a significant effect on the extracted transmission spectra. We note that the temporal window we assume for estimating the in transit spectra has the strongest effect on the extracted transmission spectra. We fix the starting time at the start of ingress (T_0-2.5 hours) and vary the transit end point from the end of the white light transit (T_0+2.5 hours), till the visual end of the He* transit (T_0+4.5 hours). The excess absorption amplitude is maximum for T_0+3.5 hours for the He* spectrum and around 3.0 hours for the Pa-α and β spectra. We explore this dependence further in Extended Data Figure 3.



Extended Data Figure 3 Effect of temporal window for categorizing in-transit and out-of-transit stellar spectra on the extracted transmission spectra for He*, Pa-α and Pa-β. We fit the extracted transmission spectra using a **Gaussian** profile for each iteration. We fix the ingress time at T_0-2.45 hours, assuming T_0=60924.268889 MJD. The horizontal axis shows the difference between the assumed end of transit and the white light curve mid transit time. We find that the amplitude of transmission spectra peaks at ∼3 hours after the white light curve mid transit time for Pa-α and β, and 3.5 hours after the white light curve mid transit time for He*. For the rest of the analysis we assume the mean and standard deviation of these fitted amplitudes — 0.25±0.02% for He*, 0.10±0.01% for Pa-α and 0.020±0.003% for Pa-β.

	Smoothed			Unsmoothed			Unsmoothed, masked		
Param	He*	Pa-α	Pa-β	He*	Pa-α	Pa-β	He*	Paα	Paβ
I_1	40.5 ± 0.5	$19.0^{+3.0}_{-4.0}$	$1.00^{+0.5}_{-1.5}$	$47.0^{+1.0}_{-1.5}$	$19.0^{+3.0}_{-3.5}$	1.00 ± 0.5	$47.0^{+4.0}_{-1.5}$	$17.5^{+2.5}_{-4.5}$	$1.00^{+3.0}_{-0.5}$
I_2	$1.50^{+0.25}_{-0.50}$	$1.00^{+0.25}_{-1.50}$	$1.25^{+0.25}_{-1.25}$	2.50 ± 0.25	1.00 ± 1.50	$1.25^{+0.25}_{-1.25}$	1.75 ± 1.25	$1.25^{+0.25}_{-1.25}$	$1.25^{+1.25}_{-0.25}$
h	1.50 ± 0.25	2.00 ± 0.50	$1.00^{+0.25}_{-0.75}$	2.25 ± 0.25	2.50 ± 1.00	$1.00^{+0.25}_{-0.75}$	2.25 ± 0.25	$2.50^{+1.0}_{-0.25}$	$1.00^{+1.5}_{-0.25}$
α	0.050 ± 0.010	$0.060^{+0.02}_{-0.01}$	$0.020^{+0.01}_{-0.05}$	0.030 ± 0.010	$0.050^{+0.01}_{-0.02}$	$0.020^{+0.01}_{-0.05}$	0.030 ± 0.010	0.060 ± 0.010	$0.020^{+0.05}_{-0.01}$

Table 1 Best-fit parameters from `harmonica` model fits to observed He*, Paα and Paβ light curves. We fit smoothed (Savitzky-Golay filter), unsmoothed and unsmoothed spot-masked models. The Paα and Paβ fits are consistent across the three fits within 1σ, however, the He* fits seem to prefer a larger escaping cloud. For the rest of the analysis we pick the smoothed model fit parameters which are the most conservative estimate from our fits. See Methods 3.2 for further details.

Code availability

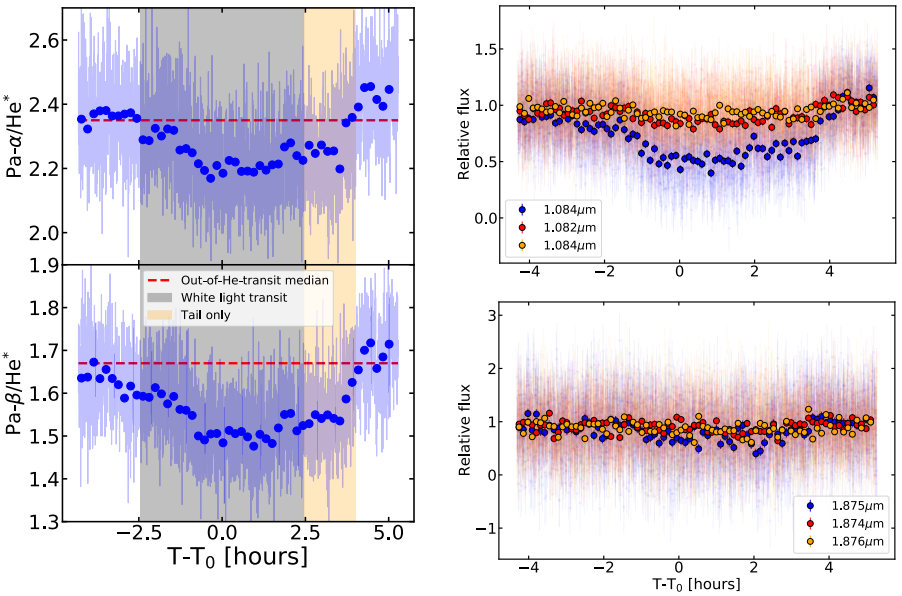
This research made use of public software like `astropy`, `batman`, `exotedrf`, `harmonica`, `sunbather` and `aiolos`.

Correspondence and request for materials

All correspondences and requests for materials related to this article should be directed to Saugata Barat (Email: saugatabarat500@gmail.com).

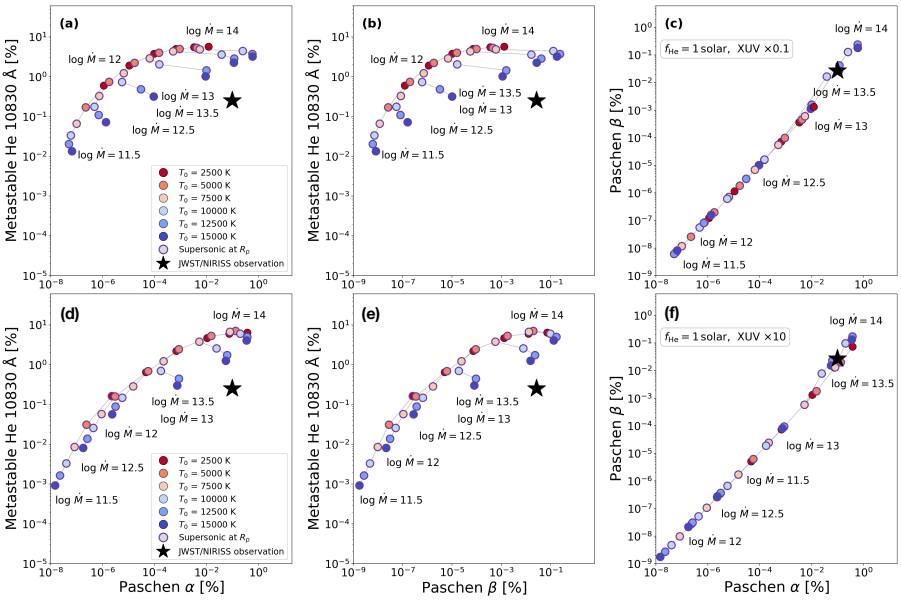
Acknowledgments

SB acknowledges the support for this program provided by NASA through a grant from the Space Telescope Science Institute, which is operated by



Extended Data Figure 4 Ratio between amplitude of the He* and Paschen lines from the 1D stellar spectra as **a** function of time(left panel) and continuum subtracted light curves for He* and Pa-α. To compute the amplitude of He* and Pa-α lines we extract a box of 25 pixels half-width centered on these lines and fit a **Gaussian** profile to the line. We find that the ratio remains constant pre-**ingress**, and returns back to that level after the He* egress. During the transit the ratios also exhibit the excess absorption feature. We find that the ratios remain consistent between the white light curve transit and the tail-only part of the transit, indicating that the attenuation of the transit depth due to the transit light source effect is not significant. **To** calculate a continuum light curve**,** we extract a light curve within this 25 pixel half-width window and subtract it from the He*(Pa-α) light curve following [45]. We also show continuum removed light curves for adjacent pixels. For the He*(Pa-α) we can again see the excess absorption in transit, and it returns back to the pre-transit level before the end of the visit. The uncertainties are propagated for both the continuum and the subtracted light curves from native resolution light curve uncertainties.

the Association of Universities for Research in Astronomy, Inc., under NASA contract NAS 5-03127. BR is supported by the National Aeronautics and Space Administration under Agreement No. 80NSSC21K0593 for the program "Alien Earths." The results reported herein benefited from collaborations and/or information exchange within NASA's Nexus for Exoplanet System Science (NExSS) research coordination network sponsored by NASA's Science Mission Directorate. This material is based upon work supported by the European Research Council (ERC) Synergy Grant under the European Union's Horizon 2020 research and innovation program (grant No. 101118581—project REVEAL). SM thanks the Heising-Simons foundation for their support through the 51 Pegasi b Fellowship. M. C. N. thanks the Heising-Simons foundation for their support through the 51 Pegasi b Fellowship. JL is partly supported by JSPS KAKENHI Grant Numbers JP24H00017 and JP25K17450.

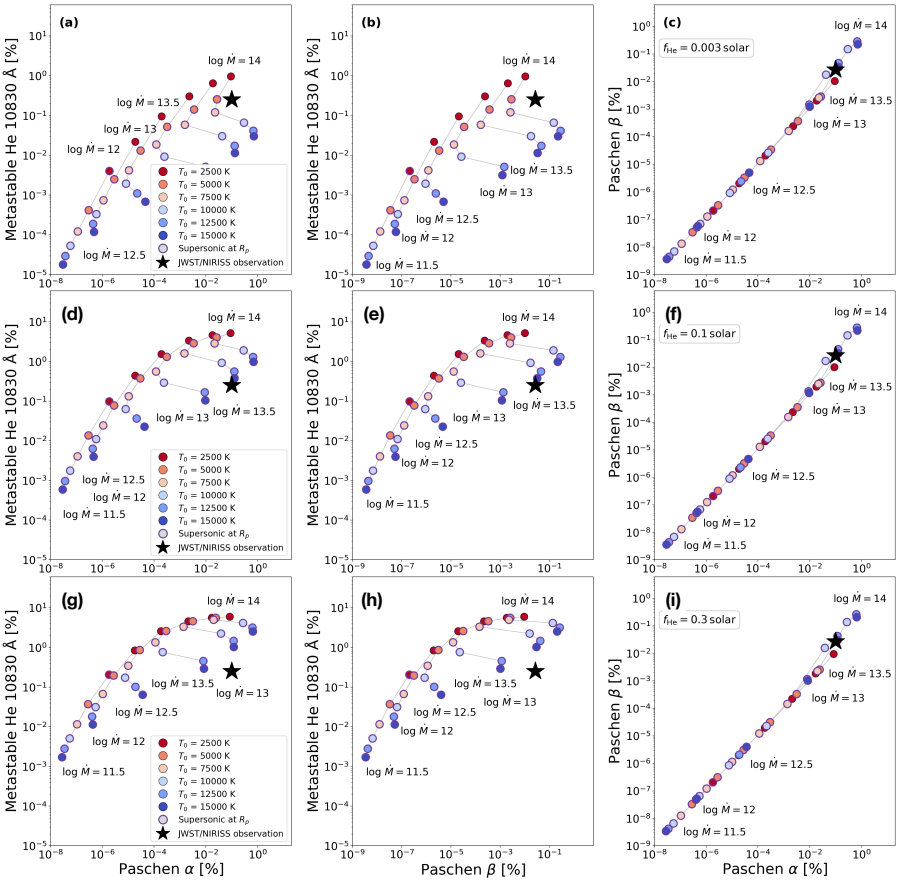


Extended Data Figure 5 Same as Figure 3 but calculated using a 0.1 times (a-c) and 10 times (d-f) the XUV flux of V1298 Tau, scaled from [66]. We find that varying the XUV flux by two orders of magnitude does not significantly **affect** the Paschen lines, but it has an effect on the He* amplitude, particularly for low mass-loss rates.

RL acknowledges financial support from the Severo Ochoa grant CEX2021-001131-S funded by MCIN/AEI/10.13039/501100011033. RL is also funded by the European Union (ERC, THIRSTEE, 101164189). Views and opinions expressed are however those of the author(s) only and do not necessarily reflect those of the European Union or the European Research Council. Neither the European Union nor the granting authority can be held responsible for them.

Authors' contributions

SB led the data analysis, manuscript preparation and overall management of the project. SV led the atmospheric escape modelling using `sunbather`. MM led the data reduction and light curve modelling using `harmonica`. WM led the atmospheric mass-loss models with `aiolos`. DS provided feedback and supported manuscript preparation. AF and LW led the proposal used to obtain these observations and provided feedback for manuscript preparation and data analysis. GD supported atmospheric modelling and manuscript feedback. SS, AV, RL, KF, BR, AM, EA, SM, MR, JMD, MN, HS and KR provided feedback for manuscript preparation. JL provided **the** ephemeris used to execute these observations and manuscript feedback.



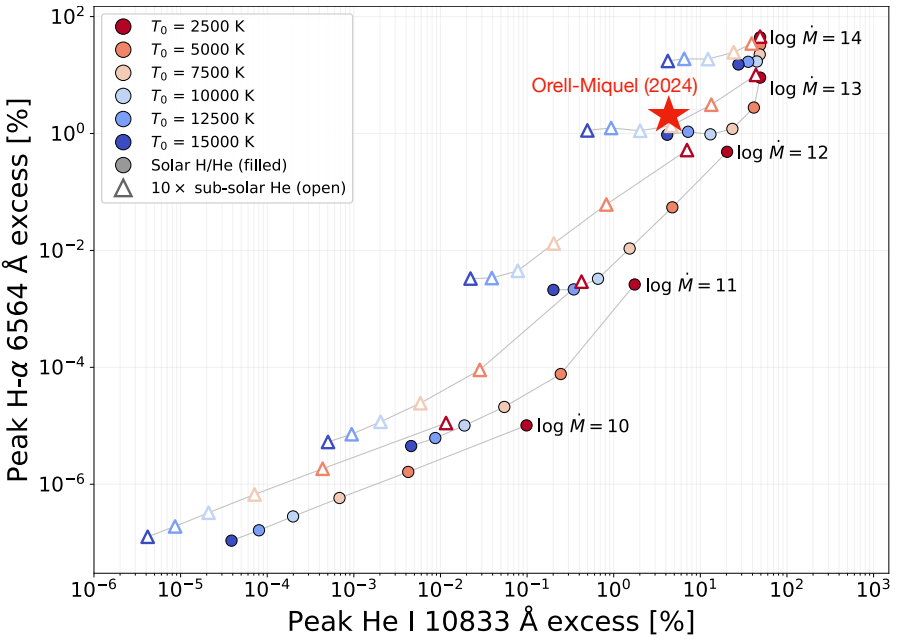
Extended Data Figure 6 Same as Figure 3 but calculated using a 0.003 times (a-c), 0.1 times (d-f) and 0.3 (g-i) times solar He/H ratio. We use the SED from [66] for these simulations. For He/H ratio of 0.003 and 0.1 solar, we can explain excess absorption signals from all three tracers, but require a mass-loss rate of 10^{14}g/s. For 0.3 solar, models over predict the He* amplitude. The Pa-α-Pa-β ratio prefers 10^{14}g/s for all simulations.

References

[1] Owen, J. E. & Wu, Y. Kepler Planets: A Tale of Evaporation. *The Astrophysical Journal* **775** (2), 105 (2013). https://doi.org/10.1088/0004-637X/775/2/105, https://arxiv.org/abs/1303.3899 [astro-ph.EP].

[2] Fulton, B. J. *et al.* The california-KeplerSurvey. III. a gap in the radius distribution of small planets. *The Astronomical Journal* **154** (3), 109 (2017). URL https://doi.org/10.3847/1538-3881/aa80eb. https://doi.org/10.3847/1538-3881/aa80eb .

[3] Livingston, J. H. *et al.* A young progenitor for the most common planetary systems in the Galaxy. *Nature* **649** (8096), 310–314 (2026). https://



Extended Data Figure 7 Modelled excess absorption of He* and H-α from our `sunbather` grids convolved to the resolution of CARMENES [100]. The red star shows the observed absorption from [57]. We show both solar and 0.1×solar He/H ratio models. The observed absorption from CARMENES matches relatively well with mass-loss rate of 10^{13} g/s model (both solar and sub-solar He/H).

doi.org/10.1038/s41586-025-09840-z, https://arxiv.org/abs/2601.10598 [astro-ph.EP].

[4] Misener, W., Schulik, M., Schlichting, H. E. & Owen, J. E. Characterizing the Bolometric-photoevaporative Transition in Young Sub-Neptunes with Radiation-hydrodynamic Simulations. *The Astrophysical Journal* **1008** (2), 184 (2026). https://doi.org/10.3847/1538-4357/ae969c, https://arxiv.org/abs/2605.02766 [astro-ph.EP].

[5] Petigura, E. A., Howard, A. W. & Marcy, G. W. Prevalence of Earth-size planets orbiting Sun-like stars. *Proceedings of the National Academy of Science* **110** (48), 19273–19278 (2013). https://doi.org/10.1073/pnas.1319909110, https://arxiv.org/abs/1311.6806 [astro-ph.EP].

[6] Buchhave, L. A. *et al.* Three regimes of extrasolar planet radius inferred from host star metallicities. *Nature* **509** (7502), 593–595 (2014). https://doi.org/10.1038/nature13254, https://arxiv.org/abs/1405.7695 [astro-ph.EP].

[7] Lee, E. J., Chiang, E. & Ormel, C. W. Make Super-Earths, Not Jupiters: Accreting Nebular Gas onto Solid Cores at 0.1 AU and Beyond. *The Astrophysical Journal* **797** (2), 95 (2014). https://doi.org/10.1088/0004-637X/797/2/95, https://arxiv.org/abs/1409.3578 [astro-ph.EP].

[8] Lee, E. J. & Chiang, E. Breeding Super-Earths and Birthing Super-puffs in Transitional Disks. *The Astrophysical Journal* **817** (2), 90 (2016). https://doi.org/10.3847/0004-637X/817/2/90, https://arxiv.org/abs/1510.08855 [astro-ph.EP].

[9] Owen, J. E. & Wu, Y. The evaporation valley in the kepler planets. *The Astrophysical Journal* **847** (1), 29 (2017). URL https://doi.org/10.3847/1538-4357/aa890a. https://doi.org/10.3847/1538-4357/aa890a .

[10] Ginzburg, S., Schlichting, H. E. & Sari, R. Core-powered mass-loss and the radius distribution of small exoplanets. *Monthly Notices of Royal Astronomical Society* **476** (1), 759–765 (2018). https://doi.org/10.1093/mnras/sty290, https://arxiv.org/abs/1708.01621 [astro-ph.EP].

[11] Gupta, A. & Schlichting, H. E. Sculpting the valley in the radius distribution of small exoplanets as a by-product of planet formation: the core-powered mass-loss mechanism. *Monthly Notices of the Royal Astronomical Society* **487** (1), 24–33 (2019). URL https://doi.org/10.1093/mnras/stz1230. https://doi.org/10.1093/mnras/stz1230, https://arxiv.org/abs/https://academic.oup.com/mnras/article-pdf/487/1/24/28693821/stz1230.pdf .

[12] Owen, J. E. & Wu, Y. Atmospheres of Low-mass Planets: The "Boil-off". *The Astrophysical Journal* **817** (2), 107 (2016). https://doi.org/10.3847/0004-637X/817/2/107, https://arxiv.org/abs/1506.02049 [astro-ph.EP].

[13] Owen, J. E. & Schlichting, H. E. Mapping out the parameter space for photoevaporation and core-powered mass-loss. *Monthly Notices of Royal Astronomical Society* **528** (2), 1615–1629 (2024). https://doi.org/10.1093/mnras/stad3972, https://arxiv.org/abs/2308.00020 [astro-ph.EP].

[14] Vach, S. *et al.* The occurrence of small, short-period planets younger than 200 Myr with TESS. *arXiv e-prints* arXiv:2403.03261 (2024). https://doi.org/10.48550/arXiv.2403.03261, https://arxiv.org/abs/2403.03261 [astro-ph.EP].

[15] Rogers, J. G. On the road to the radius valley: distinguishing between gas dwarfs and water worlds with young transiting exoplanets. *Monthly Notices of Royal Astronomical Society* **539** (3), 2230–2241 (2025). https://doi.org/10.1093/mnras/staf628, https://arxiv.org/abs/2503.17364 [astro-ph.EP].

[16] Barat, S. *et al.* The metal-poor atmosphere of a potential sub-Neptune progenitor. *Nature Astronomy* **8**, 899–908 (2024). https://doi.org/10.1038/s41550-024-02257-0, https://arxiv.org/abs/2312.16924 [astro-ph.EP].

[17] Thao, P. C. *et al.* The Featherweight Giant: Unraveling the Atmosphere of a 17 Myr Planet with JWST. *arXiv e-prints* arXiv:2409.16355 (2024). https://doi.org/10.48550/arXiv.2409.16355, https://arxiv.org/abs/2409.16355 [astro-ph.EP].

[18] Barat, S. *et al.* A Metal-poor Atmosphere with a Hot Interior for a Young Sub-Neptune Progenitor: JWST/NIRSpec Transmission Spectrum of V1298 Tau b. *Astronomical Journal* **170** (3), 165 (2025). https://doi.org/10.3847/1538-3881/adec89, https://arxiv.org/abs/2507.08837 [astro-ph.EP].

[19] Murphy, M. M. *et al.* Kronos i: The $1-2.8\mu$m jwst transmission spectrum of the 23 myr v1298 tau c (2026). URL https://arxiv.org/abs/2606.03740. 2606.03740.

[20] Vidal-Madjar, A. *et al.* An extended upper atmosphere around the extrasolar planet HD209458b. *Nature* **422** (6928), 143–146 (2003). https://doi.org/10.1038/nature01448 .

[21] France, K. *et al.* The Ultraviolet Radiation Environment around M dwarf Exoplanet Host Stars. *The Astrophysical Journal* **763** (2), 149 (2013). https://doi.org/10.1088/0004-637X/763/2/149, https://arxiv.org/abs/1212.4833 [astro-ph.EP].

[22] Ehrenreich, D. *et al.* A giant comet-like cloud of hydrogen escaping the warm Neptune-mass exoplanet GJ 436b. *Nature* **522** (7557), 459–461 (2015). https://doi.org/10.1038/nature14501, https://arxiv.org/abs/1506.07541 [astro-ph.EP].

[23] Bourrier, V. *et al.* Hubble PanCET: an extended upper atmosphere of neutral hydrogen around the warm Neptune GJ 3470b. *Astronomy & Astrophysics* **620**, A147 (2018). https://doi.org/10.1051/0004-6361/201833675, https://arxiv.org/abs/1812.05119 [astro-ph.EP].

[24] Jensen, A. G. *et al.* A Detection of Hα in an Exoplanetary Exosphere. *The Astrophysical Journal* **751** (2), 86 (2012). https://doi.org/10.1088/0004-637X/751/2/86, https://arxiv.org/abs/1203.4484 [astro-ph.EP].

[25] Seager, S. & Sasselov, D. D. Theoretical Transmission Spectra during Extrasolar Giant Planet Transits. *The Astrophysical Journal* **537** (2), 916–921 (2000). https://doi.org/10.1086/309088, https://arxiv.org/abs/astro-ph/9912241 [astro-ph].

[26] Oklopčić, A. & Hirata, C. M. A New Window into Escaping Exoplanet Atmospheres: 10830 Å Line of Helium. *Astrophysical Journal Letters* **855** (1), L11 (2018). https://doi.org/10.3847/2041-8213/aaada9, https://arxiv.org/abs/1711.05269 [astro-ph.EP].

[27] Vissapragada, S., Knutson, H. A., dos Santos, L. A., Wang, L. & Dai, F. The Maximum Mass-loss Efficiency for a Photoionization-driven Isothermal Parker Wind. *The Astrophysical Journal* **927** (1), 96 (2022). https://doi.org/10.3847/1538-4357/ac4e8a, https://arxiv.org/abs/2201.09889 [astro-ph.EP].

[28] Linssen, D. C., Oklopčić, A. & MacLeod, M. Constraining planetary mass-loss rates by simulating Parker wind profiles with Cloudy. *Astronomy & Astrophysics* **667**, A54 (2022). https://doi.org/10.1051/0004-6361/202243830, https://arxiv.org/abs/2209.03677 [astro-ph.EP].

[29] Masson, A. *et al.* Probing atmospheric escape through metastable He I triplet lines in 15 exoplanets observed with SPIRou. *Astronomy & Astrophysics* **688**, A179 (2024). https://doi.org/10.1051/0004-6361/202449608, https://arxiv.org/abs/2406.09225 [astro-ph.EP].

[30] Taylor, A. R. *et al.* A Multispecies Atmospheric Escape Model with Excited Hydrogen and Helium: Application to HD209458b. *The Astrophysical Journal* **989** (1), 68 (2025). https://doi.org/10.3847/1538-4357/ade3c9, https://arxiv.org/abs/2506.08232 [astro-ph.EP].

[31] Nortmann, L. *et al.* Ground-based detection of an extended helium atmosphere in the Saturn-mass exoplanet WASP-69b. *Science* **362** (6421), 1388–1391 (2018). https://doi.org/10.1126/science.aat5348, https://arxiv.org/abs/1812.03119 [astro-ph.EP].

[32] Allart, R. *et al.* Spectrally resolved helium absorption from the extended atmosphere of a warm Neptune-mass exoplanet. *Science* **362** (6421), 1384–1387 (2018). https://doi.org/10.1126/science.aat5879, https://arxiv.org/abs/1812.02189 [astro-ph.EP].

[33] Salz, M. *et al.* Detection of He I λ10830 Å absorption on HD 189733 b with CARMENES high-resolution transmission spectroscopy. *Astronomy & Astrophysics* **620**, A97 (2018). https://doi.org/10.1051/0004-6361/201833694, https://arxiv.org/abs/1812.02453 [astro-ph.EP].

[34] Hirano, T. *et al.* Limits on the Spin-Orbit Angle and Atmospheric Escape for the 22 Myr Old Planet AU Mic b. *Astrophysical Journal Letters* **899** (1), L13 (2020). https://doi.org/10.3847/2041-8213/aba6eb, https://arxiv.org/abs/2006.13243 [astro-ph.EP].

[35] Vissapragada, S. *et al.* A Search for Planetary Metastable Helium Absorption in the V1298 Tau System. *arXiv e-prints* arXiv:2108.05358 (2021). https://arxiv.org/abs/2108.05358 [astro-ph.EP].

[36] Alam, M. K. *et al.* The First Near-infrared Transmission Spectrum of HIP 41378 f, A Low-mass Temperate Jovian World in a Multiplanet System. *Astrophysical Journal Letters* **927** (1), L5 (2022). https://doi.org/10.3847/2041-8213/ac559d, https://arxiv.org/abs/2201.02686 [astro-ph.EP].

[37] Milburn, R. P. *et al.* Ever Elusive Exospheres: One Probable Detection and Two Nondetections of Hα Transits in Young Systems. *Astronomical Journal* **170** (6), 348 (2025). https://doi.org/10.3847/1538-3881/ae1504, https://arxiv.org/abs/2510.18820 [astro-ph.EP].

[38] Hirano, T. *et al.* Transit spectroscopy of K2-33b with subaru/IRD: Spin-Orbit alignment and tentative atmospheric helium. *Monthly Notices of Royal Astronomical Society* **530** (3), 3117–3126 (2024). https://doi.org/10.1093/mnras/stae998, https://arxiv.org/abs/2404.07262 [astro-ph.EP].

[39] Plavchan, P. *et al.* A planet within the debris disk around the pre-main-sequence star AU Microscopii. *Nature* **582** (7813), 497–500 (2020). https://doi.org/10.1038/s41586-020-2400-z, https://arxiv.org/abs/2006.13248 [astro-ph.EP].

[40] Rockcliffe, K. E. *et al.* The Variable Detection of Atmospheric Escape around the Young, Hot Neptune AU Mic b. *Astronomical Journal* **166** (2), 77 (2023). https://doi.org/10.3847/1538-3881/ace536, https://arxiv.org/abs/2307.15024 [astro-ph.EP].

[41] Krolikowski, D. M. *et al.* The Strength and Variability of the Helium 10830 Å Triplet in Young Stars, with Implications for Exosphere Detection. *Astronomical Journal* **167** (2), 79 (2024). https://doi.org/10.3847/1538-3881/ad0f22, https://arxiv.org/abs/2311.04971 [astro-ph.SR].

[42] Zhang, Z. *et al.* Giant tidal tails of helium escaping the hot Jupiter HAT-P-32 b. *Science Advances* **9** (23), eadf8736 (2023). https://doi.org/10.1126/sciadv.adf8736, https://arxiv.org/abs/2306.03913 [astro-ph.EP].

[43] Gully-Santiago, M. *et al.* A Large and Variable Leading Tail of Helium in a Hot Saturn Undergoing Runaway Inflation. *Astronomical Journal* **167** (4), 142 (2024). https://doi.org/10.3847/1538-3881/ad1ee8, https://arxiv.org/abs/2307.08959 [astro-ph.EP].

[44] Allart, R. *et al.* A complex structure of escaping helium spanning more than half the orbit of the ultra-hot Jupiter WASP-121\,b. *arXiv*

e-prints arXiv:2510.09809 (2025). https://arxiv.org/abs/2510.09809 [astro-ph.EP].

[45] Krishnamurthy, V. *et al.* Continuous helium absorption from both the leading and trailing tails of WASP-107 b. *Nature Astronomy* **10**, 258–270 (2026). https://doi.org/10.1038/s41550-025-02710-8, https://arxiv.org/abs/2505.20588 [astro-ph.EP].

[46] Spake, J. J. *et al.* Helium in the eroding atmosphere of an exoplanet. *Nature* **557** (7703), 68–70 (2018). https://doi.org/10.1038/s41586-018-0067-5, https://arxiv.org/abs/1805.01298 [astro-ph.EP].

[47] Fu, G. *et al.* Water and an Escaping Helium Tail Detected in the Hazy and Methane-depleted Atmosphere of HAT-P-18b from JWST NIRISS/SOSS. *Astrophysical Journal Letters* **940** (2), L35 (2022). https://doi.org/10.3847/2041-8213/ac9977, https://arxiv.org/abs/2211.13761 [astro-ph.EP].

[48] Fournier-Tondreau, M. *et al.* Near-infrared transmission spectroscopy of HAT-P-18 b with NIRISS: Disentangling planetary and stellar features in the era of JWST. *Monthly Notices of Royal Astronomical Society* **528** (2), 3354–3377 (2024). https://doi.org/10.1093/mnras/stad3813, https://arxiv.org/abs/2310.14950 [astro-ph.EP].

[49] Ahrer, E.-M. *et al.* Escaping Helium and a Highly Muted Spectrum Suggest a Metal-enriched Atmosphere on Sub-Neptune GJ 3090 b from JWST Transit Spectroscopy. *Astrophysical Journal Letters* **985** (1), L10 (2025). https://doi.org/10.3847/2041-8213/add010, https://arxiv.org/abs/2504.20428 [astro-ph.EP].

[50] Feinstein, A. *et al.* KRONOS: Keys to Revealing the Origin and Nature Of sub-neptune Systems. JWST Proposal. Cycle 3, ID. #5959 (2024).

[51] David, T. J. *et al.* Four Newborn Planets Transiting the Young Solar Analog V1298 Tau. *Astrophysical Journal Letters* **885** (1), L12 (2019). https://doi.org/10.3847/2041-8213/ab4c99, https://arxiv.org/abs/1910.04563 [astro-ph.EP].

[52] Barat, S. *et al.* First Comparative Exoplanetology Within a Transiting Multi-planet System: Comparing the atmospheres of V1298 Tau b and c. *arXiv e-prints* arXiv:2407.14995 (2024). https://doi.org/10.48550/arXiv.2407.14995, https://arxiv.org/abs/2407.14995 [astro-ph.EP].

[53] Benneke, B. *et al.* JWST Reveals CH_4, CO_2, and H_2O in a Metal-rich Miscible Atmosphere on a Two-Earth-Radius Exoplanet. *arXiv e-prints* arXiv:2403.03325 (2024). https://doi.org/10.48550/arXiv.2403.03325, https://arxiv.org/abs/2403.03325 [astro-ph.EP].

[54] Beatty, T. G. *et al.* Sulfur Dioxide and Other Molecular Species in the Atmosphere of the Sub-Neptune GJ 3470 b. *arXiv e-prints* arXiv:2406.04450 (2024). https://doi.org/10.48550/arXiv.2406.04450, https://arxiv.org/abs/2406.04450 [astro-ph.EP].

[55] Barat, S. *et al.* JWST Unveils a High Mean Molecular Weight Atmosphere for Mini-Neptune TOI-1130 b: Evidence for Formation Beyond the Water Ice Line. *Astrophysical Journal Letters* **1002** (2), L32 (2026). https://doi.org/10.3847/2041-8213/ae5f8b, https://arxiv.org/abs/2605.02036 [astro-ph.EP].

[56] Alam, M. K. *et al.* Nondetections of Helium in the Young Sub-Jovian Planets K2-100b, HD 63433b, and V1298 Tau c. *Astronomical Journal* **168** (3), 102 (2024). https://doi.org/10.3847/1538-3881/ad50d4, https://arxiv.org/abs/2405.17294 [astro-ph.EP].

[57] Orell-Miquel, J. *et al.* The MOPYS project: A survey of 70 planets in search of extended He I and H atmospheres: No evidence of enhanced evaporation in young planets. *Astronomy & Astrophysics* **689**, A179 (2024). https://doi.org/10.1051/0004-6361/202449411, https://arxiv.org/abs/2404.16732 [astro-ph.EP].

[58] Feinstein, A. D., France, K., Cauley, P. W. & Livingston, J. H. HST Far-ultraviolet Transit Observations of Two Neptune Progenitors Younger than 30 Myr. *Research Notes of the American Astronomical Society* **8** (3), 86 (2024). https://doi.org/10.3847/2515-5172/ad35b7 .

[59] Grant, D. & Wakeford, H. R. Transmission strings: a technique for spatially mapping exoplanet atmospheres around their terminators. *Monthly Notices of the Royal Astronomical Society* **519** (4), 5114–5127 (2023) .

[60] Gascón, C. *et al.* Modeling tails of escaping gas in exoplanet atmospheres with Harmonica. *The Astrophysical Journal Letters* **991** (2), L47 (2025). URL http://arxiv.org/abs/2508.14846. https://doi.org/10.3847/2041-8213/adfb77, arXiv:2508.14846 [astro-ph] .

[61] Murphy, M. M. *et al.* KRONOS II: Solar-like Umbra and Penumbra Properties on the Young Sun V1298. *arXiv e-prints* arXiv:2606.16782 (2026). https://doi.org/10.48550/arXiv.2606.16782, https://arxiv.org/abs/2606.16782 [astro-ph.SR].

[62] Wang, L. & Dai, F. Metastable Helium Absorptions with 3D Hydrodynamics and Self-consistent Photochemistry. II. WASP-107b, Stellar Wind, Radiation Pressure, and Shear Instability. *The Astrophysical Journal* **914** (2), 99 (2021). https://doi.org/10.3847/1538-4357/abf1ed, https://arxiv.org/abs/2101.00045 [astro-ph.EP].

[63] Sánchez-López, A. *et al.* Detection of Paschen β absorption in the atmosphere of KELT-9 b. A new window into the atmospheres of ultra-hot Jupiters. *Astronomy & Astrophysics* **666**, L1 (2022). https://doi.org/10.1051/0004-6361/202244416, https://arxiv.org/abs/2209.01854 [astro-ph.EP].

[64] Schlawin, E. *et al.* JWST Noise Floor. I. Random Error Sources in JWST NIRCam Time Series. *Astronomical Journal* **160** (5), 231 (2020). https://doi.org/10.3847/1538-3881/abb811, https://arxiv.org/abs/2010.03564 [astro-ph.IM].

[65] Linssen, D., Shih, J., MacLeod, M. & Oklopčić, A. The open-source sunbather code: Modeling escaping planetary atmospheres and their transit spectra. *Astronomy & Astrophysics* **688**, A43 (2024). https://doi.org/10.1051/0004-6361/202450240, https://arxiv.org/abs/2404.12775 [astro-ph.EP].

[66] Duvvuri, G. M. *et al.* The High-energy Spectrum of the Young Planet Host V1298 Tau. *Astronomical Journal* **166** (5), 196 (2023). https://doi.org/10.3847/1538-3881/acfa74, https://arxiv.org/abs/2310.00155 [astro-ph.SR].

[67] Dos Santos, L. A. *et al.* p-winds: An open-source Python code to model planetary outflows and upper atmospheres. *Astronomy & Astrophysics* **659**, A62 (2022). https://doi.org/10.1051/0004-6361/202142038, https://arxiv.org/abs/2111.11370 [astro-ph.EP].

[68] Ferland, G. J. *et al.* CLOUDY 90: Numerical Simulation of Plasmas and Their Spectra. *Publications of Astronomical Society of the Pacific* **110** (749), 761–778 (1998). https://doi.org/10.1086/316190 .

[69] Mansfield, M. *et al.* Detection of Helium in the Atmosphere of the Exo-Neptune HAT-P-11b. *Astrophysical Journal Letters* **868** (2), L34 (2018). https://doi.org/10.3847/2041-8213/aaf166, https://arxiv.org/abs/1812.02214 [astro-ph.EP].

[70] Cherubim, C., Wordsworth, R., Hu, R. & Shkolnik, E. Strong Fractionation of Deuterium and Helium in Sub-Neptune Atmospheres along the Radius Valley. *The Astrophysical Journal* **967** (2), 139 (2024). https://doi.org/10.3847/1538-4357/ad3e77, https://arxiv.org/abs/2402.10690 [astro-ph.EP].

[71] Saidel, M. *et al.* Stringent Upper Bounds on Atmospheric Mass Loss from Three Neptune-sized Planets in the TOI-4010 System. *Astronomical Journal* **170** (4), 247 (2025). https://doi.org/10.3847/1538-3881/adfe5e, https://arxiv.org/abs/2508.21166 [astro-ph.EP].

[72] García Muñoz, A. Modeling helium in exoplanet atmospheres. A revised network with photoelectron-driven processes. *Astronomy & Astrophysics* **698**, A199 (2025). https://doi.org/10.1051/0004-6361/202555145, https://arxiv.org/abs/2505.12148 [astro-ph.EP].

[73] Taylor, A. R., Koskinen, T. T., Huang, C., Arfaux, A. & Lavvas, P. Helium Escape in Context: Comparative Signatures of Four Close-in Exoplanets. *The Astrophysical Journal* **999** (2), 214 (2026). https://doi.org/10.3847/1538-4357/ae41b5, https://arxiv.org/abs/2602.02289 [astro-ph.EP].

[74] Rumenskikh, M. S. *et al.* Mysterious non-detection of He I (2^3S) transit absorption of GJ 436b. *Monthly Notices of Royal Astronomical Society* **526** (3), 4120–4129 (2023). https://doi.org/10.1093/mnras/stad2846, https://arxiv.org/abs/2401.11938 [astro-ph.EP].

[75] France, K. *et al.* A Semiempirical Estimate of Solar Extreme-ultraviolet Evolution from 10 Myr to 10 Gyr. *Astronomical Journal* **170** (3), 159 (2025). https://doi.org/10.3847/1538-3881/adefdf, https://arxiv.org/abs/2507.15953 [astro-ph.SR].

[76] Louca, A. & Miguel, Y. Metal-Enriched Atmospheres in Warm (Super- and Sub-)Neptunes Induced by Extreme Atmospheric Escape. *arXiv e-prints* arXiv:2505.06013 (2025). https://doi.org/10.48550/arXiv.2505.06013, https://arxiv.org/abs/2505.06013 [astro-ph.EP].

[77] Valatsou, M., Dorn, C., Marty, P. & Owen, J. E. Oxygen left behind: Atmospheric Enrichment due to Fractionation in Sub-Neptunes using BOREAS. *arXiv e-prints* arXiv:2602.12201 (2026). https://doi.org/10.48550/arXiv.2602.12201, https://arxiv.org/abs/2602.12201 [astro-ph.EP].

[78] Kite, E. S., Fegley, B., Jr., Schaefer, L. & Ford, E. B. Atmosphere Origins for Exoplanet Sub-Neptunes. *The Astrophysical Journal* **891** (2), 111 (2020). https://doi.org/10.3847/1538-4357/ab6ffb, https://arxiv.org/abs/2001.09269 [astro-ph.EP].

[79] Werlen, A. *et al.* Sub-Neptunes Are Drier than They Seem: Rethinking the Origins of Water-rich Worlds. *Astrophysical Journal Letters* **991** (1), L16 (2025). https://doi.org/10.3847/2041-8213/adff73, https://arxiv.org/abs/2507.00765 [astro-ph.EP].

[80] Steinmeyer, M.-L., Dorn, C., Werlen, A. & Grimm, S. L. Coupled Thermal-Chemical Evolution Models of Sub-Neptunes Reveal Atmospheric Signatures of Their Formation Location. *The Astrophysical Journal* **1001** (1), 36 (2026). https://doi.org/10.3847/1538-4357/ae4c47, https://arxiv.org/abs/2601.21377 [astro-ph.EP].

[81] Dai, F. *et al.* Photochemical CS_2 Gas Detected on a 20-Myr-old Exoplanet. *arXiv e-prints* arXiv:2606.00974 (2026). https://doi.org/10.48550/arXiv.2606.00974, https://arxiv.org/abs/2606.00974 [astro-ph.EP].

[82] Yoshida, T. & Gaidos, E. Water-cooled (sub)-Neptunes get better gas mileage. *Astronomy & Astrophysics* **696**, L13 (2025). https://doi.org/10.1051/0004-6361/202553667, https://arxiv.org/abs/2503.23020 [astro-ph.EP].

[83] Kubyshkina, D., Egger, J. A. & Piaulet-Ghorayeb, C. Escape of Water- and Metal-enriched Atmospheres from compact Hot mini-Neptunes with CHAIN. *arXiv e-prints* arXiv:2606.02083 (2026). https://doi.org/10.48550/arXiv.2606.02083, https://arxiv.org/abs/2606.02083 [astro-ph.EP].

[84] Schulik, M. & Booth, R. A. AIOLOS - A multipurpose 1D hydrodynamics code for planetary atmospheres. *Monthly Notices of Royal Astronomical Society* **523** (1), 286–304 (2023). https://doi.org/10.1093/mnras/stad1251, https://arxiv.org/abs/2207.07144 [astro-ph.EP].

[85] Doyon, R. *et al.* The Near Infrared Imager and Slitless Spectrograph for the James Webb Space Telescope. I. Instrument Overview and In-flight Performance. *Publications of Astronomical Society of the Pacific* **135** (1051), 098001 (2023). https://doi.org/10.1088/1538-3873/acd41b, https://arxiv.org/abs/2306.03277 [astro-ph.IM].

[86] Radica, M. exoTEDRF: An EXOplanet Transit and Eclipse Data Reduction Framework. *The Journal of Open Source Software* **9** (100), 6898 (2024). https://doi.org/10.21105/joss.06898, https://arxiv.org/abs/2407.17541 [astro-ph.IM].

[87] Coulombe, L.-P. *et al.* A broadband thermal emission spectrum of the ultra-hot Jupiter WASP-18b. *Nature* **620** (7973), 292–298 (2023). https://doi.org/10.1038/s41586-023-06230-1, https://arxiv.org/abs/2301.08192 [astro-ph.EP].

[88] Avni, Y. Energy spectra of X-ray clusters of galaxies. *The Astrophysical Journal* **210**, 642–646 (1976). https://doi.org/10.1086/154870 .

[89] Rackham, B. V., Apai, D. & Giampapa, M. S. The Transit Light Source Effect. II. The Impact of Stellar Heterogeneity on Transmission Spectra of Planets Orbiting Broadly Sun-like Stars. *Astronomical Journal* **157** (3), 96 (2019). https://doi.org/10.3847/1538-3881/aaf892, https://arxiv.org/abs/1812.06184 [astro-ph.EP].

[90] Wiese, W. L. & Fuhr, J. R. Accurate Atomic Transition Probabilities for Hydrogen, Helium, and Lithium. *Journal of Physical and Chemical Reference Data* **38** (3), 565–720 (2009). https://doi.org/10.1063/1.3077727 .

[91] Rybicki, G. B. & Lightman, A. P. *Radiative processes in astrophysics* (1979).

[92] Wiese, W. L. & Fuhr, J. R. Accurate Atomic Transition Probabilities for Hydrogen, Helium, and Lithium. *Journal of Physical and Chemical Reference Data* **38** (3), 565–720 (2009). https://doi.org/10.1063/1.3077727 .

[93] Dos Santos, L. A. *et al.* p-winds: An open-source Python code to model planetary outflows and upper atmospheres. *Astronomy & Astrophysics* **659**, A62 (2022). https://doi.org/10.1051/0004-6361/202142038, https://arxiv.org/abs/2111.11370 [astro-ph.EP].

[94] Ferland, G. J. *et al.* CLOUDY 90: Numerical Simulation of Plasmas and Their Spectra. *Publications of Astronomical Society of the Pacific* **110** (749), 761–778 (1998). https://doi.org/10.1086/316190 .

[95] Ferland, G. J. *et al.* The 2017 Release Cloudy. *Revista Mexicana de Astronomía y Astrofísica* **53**, 385–438 (2017). https://doi.org/10.48550/arXiv.1705.10877, https://arxiv.org/abs/1705.10877 [astro-ph.GA].

[96] Chatzikos, M. *et al.* The 2023 Release of Cloudy. *Revista Mexicana de Astronomía y Astrofísica* **59**, 327–343 (2023). https://doi.org/10.22201/ia.01851101p.2023.59.02.12, https://arxiv.org/abs/2308.06396 [astro-ph.GA].

[97] Sethi, R., MacLeod, M. & Millholland, S. Atmospheric Escape Rates of Planets in Stellar Tidal Fields from 3D Hydrodynamic Simulations. *The Astrophysical Journal* **1008** (1), 11 (2026). https://doi.org/10.3847/1538-4357/ae9155, https://arxiv.org/abs/2607.24733 [astro-ph.EP].

[98] Feinstein, A. D. *et al.* H-alpha and Ca II Infrared Triplet Variations During a Transit of the 23 Myr Planet V1298 Tau c. *Astronomical Journal* **162** (5), 213 (2021). https://doi.org/10.3847/1538-3881/ac1f24, https://arxiv.org/abs/2107.01213 [astro-ph.EP].

[99] Schlawin, E. *et al.* H-alpha Variability of V1298 Tau c. *Research Notes of the American Astronomical Society* **5** (8), 195 (2021). https://doi.org/10.3847/2515-5172/ac1f2f, https://arxiv.org/abs/2108.08851 [astro-ph.EP].

[100] Quirrenbach, A. *et al.* Evans, C. J., Simard, L. & Takami, H. (eds) *CARMENES: high-resolution spectra and precise radial velocities in the red and infrared.* (eds Evans, C. J., Simard, L. & Takami, H.) *Ground-based and Airborne Instrumentation for Astronomy VII*, Vol. 10702 of *Society of Photo-Optical Instrumentation Engineers (SPIE) Conference Series*, 107020W (2018).